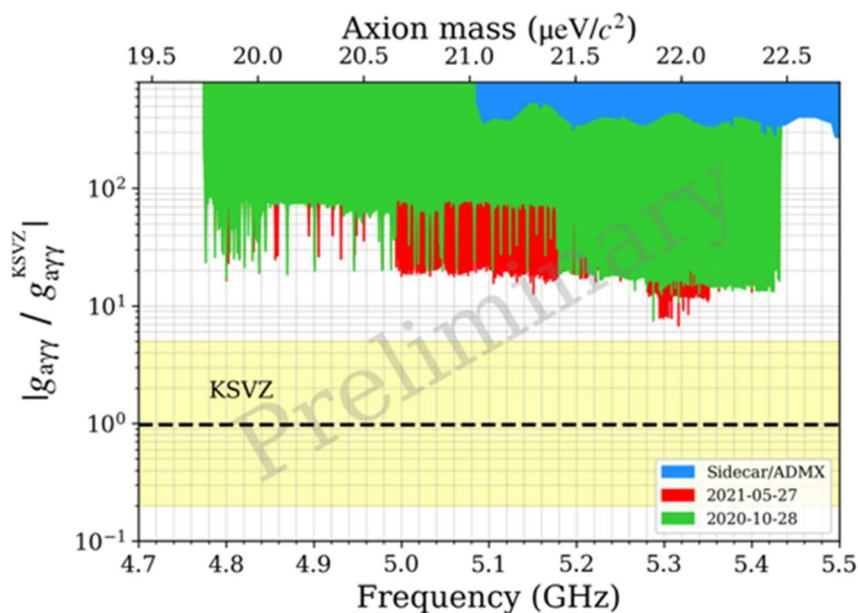


# CAST

## Status Report to the SPSC for the 142<sup>nd</sup> Meeting



CERN, May 28, 2021

**On behalf of the CAST Collaboration,**

**Editor: Horst Fischer**

Albert-Ludwigs-Universität Freiburg  
Physikalisches Institut  
Hermann-Herder-Str. 3  
79104 Freiburg im Brsg.





## Table of Contents

1	Technical Coordination: Status of CAST Infrastructure.....	1
1.1	2020 data taking campaign .....	1
1.2	2021 data taking campaign .....	1
2	CAST-CAPP – Wide band dark matter axion search .....	1
2.1	Summary .....	1
2.2	Data taking campaign 2020/2021 .....	2
2.2.1	Measurements with single cavities .....	2
2.2.2	Phase Matching .....	2
2.3	DAQ system and strategies .....	3
2.3.1	DAQ chain .....	3
2.3.2	Identifying electromagnetic interferences .....	5
2.3.3	Signal injections .....	6
2.3.4	Fast Resonant Frequency Tuning.....	7
2.4	Data Analysis .....	7
2.4.1	Parameters optimization.....	7
2.4.2	Noise distribution cross-checks .....	10
2.4.3	Quality checks.....	11
2.4.4	Results and outliers .....	11
2.5	Future Prospects .....	12
2.6	Concluding Remark .....	13
3	RADES – High-mass axion search .....	19
3.1	Developments since October 2020 .....	19
3.1.1	Submission of 2018 data-taking results for publication.....	19
3.1.2	Data-taking 2020-2021 .....	19
3.2	Future possibilities for RADES in CAST .....	20
4	The new solar axion data taking campaign with the IAXO pathfinder system at CAST .....	20
4.1	Summary and goals .....	20
4.2	Preliminary considerations.....	21
4.3	Status and achievements .....	21
4.4	Data taking campaign with Xe-based mixtures .....	21
4.5	Data analysis .....	22
4.6	Preliminary background spectrum with Xenon .....	23
4.7	Low gain runs.....	23
5	InGrid/GridPix detector – Search for low energy solar ALPS .....	24
5.1	Stability of energy calibration.....	24
5.2	Optimization of energy-dependent likelihood selection .....	25
5.3	Advancement towards more modern statistical interpretation (profile likelihood) .....	25
5.4	Further improvements .....	26
6	KWISP – Chameleon Search with an opto-mechanical detector.....	26
6.1	Introduction.....	26
6.2	KWISP 3.5 set-up .....	26
6.3	Recent upgrades .....	27
6.4	Data taking .....	28
6.5	Results.....	28
6.6	Conclusions.....	30



# 1 Technical Coordination: Status of CAST Infrastructure

## 1.1 2020 data taking campaign

In 2020 the magnet was on for a total of 2635 hours. In particular, between the 24th of September and the 16th of December 2020 the magnet was on for 1277 hours and, parasitically, we followed the sun during 51 hours without interfering with the DM axion search.

## 1.2 2021 data taking campaign

In early 2021 it was foreseen that the magnet would be cooled down immediately after the Christmas break as no mechanical or vacuum interventions were foreseen. In the beginning of 2021 we performed a network upgrade which considerably increased the data transfer speed and we also migrated from CASTOR data archiving to CTA, but this run in parallel with the CAST planning.

In the beginning of 2021 it was reported that the piezo mechanism of one of the CAPP cavities was not responding. In an attempt to restore its functionality, on the 7th of January we started actively warming up the magnet, which was passively warming up since the 16th of December. Until the 17th of January when we reached almost 295 K, the piezo was not restored. We then started cooling down on the 18th of January. After the quench training, the magnet was ramped up for the first time for physics data taking campaign on the 28th of January 2021.

The 2021 data taking campaign was relatively uneventful. We have had two quenches, a natural one on the 7th of February and one on the 16th of March. The latter was caused by power tests on the LHC magnets at P8 which caused an overload of 400V consumption on the ERD1 / 8R and ERD2 / 8R panels. The HV protection relay measured this overload and tripped causing the quench.

In total (until 18/5/2021) the magnet was on for 2509 hours. We did 56 solar tracking and the magnet followed the sun for 84 hours. The data taking hours per detector and the issues of each detector system will be detailed in the corresponding chapters.

# 2 CAST-CAPP – Wide band dark matter axion search

## 2.1 Summary

The CAST-CAPP sub-detector is using 4 microwave cavities searching for Dark Matter axions thus transforming the CAST experiment from an axion helioscope to an axion haloscope. During the last months, CAST-CAPP improved its statistical sensitivity having now in total ~153 days of data with magnetic field ON and focused on the analysis of the data. These soon-to-be-published data in the range 19.7 to 22.4  $\mu\text{eV}$  (4.7 to 5.5 GHz) allow for a significant increase in sensitivity, exceeding previous measurements by almost two orders of magnitude. The upgrade of the DAQ chain and the progress in the analysis were crucial to gain a rejection power against electromagnetic parasites. CAST-CAPP has pioneered a new technology and data-taking strategy, in addition to halo dark matter axions, through fast resonance scanning and phase-matching of multiple cavities that allows to search also for transient events. Furthermore, the experience gained with phase matching allows to project applications in future large scale axion haloscopes like that of the IAXO project.

An extension of the data taking time will allow CAST-CAPP to improve its own cutting-edge limits on the axion-photon coupling for a relatively wide range of axion masses. Envisioning continued operation for 12 months of data taking, the sensitivity will reach into the band of theoretical predictions in a yet unexplored mass range.

## 2.2 Data taking campaign 2020/2021

Since the presentation to the SPSC committee (13/10/2020), the CAST-CAPP sub-detector has taken data in the periods from 23/11/2020 to 16/12/2020 and continuously since 02/02/2021 until today. The current total acquired data up to 26/05/2021 correspond to 3670.3 hours (152.9 days) for ~ 660 MHz range. This corresponds to a duty cycle of about 16.2 hours/day for the latest runs, with 20 hours/day being the maximum possible rate. The covered frequency range with all cavities is 660.15 MHz from 4.7739 GHz to 5.4341GHz.

### 2.2.1 Measurements with single cavities

The data-taking time using CAST-CAPP cavities individually is 2126.6 hours (86.6 days). The frequency ranges accessible by the individual CAST-CAPP cavities are:

- Cavity 1: 127.6MHz (5.2224 GHz – 5.3500 GHz)
- Cavity 2: 199.0MHz (5.1823 GHz – 5.3813 GHz)
- Cavity 3: 211.7MHz (5.2224 GHz – 5.4341 GHz)
- Cavity 4: 471.9MHz (4.7740 GHz – 5.2459 GHz)

Please note, single manual intervention to the locomotive gear drive enables the scanning of a frequency range extended by a factor of two.

### 2.2.2 Phase Matching

To increase the effective volume of the CAST-CAPP detector, and therefore its sensitivity, multiple cavities instead of enlarging a single cavity are used. Further enhancement of the signal-to-noise ratio (SNR) is made through the “phase matching” technique by combining coherently the power outputs of each frequency-matched cavity after individual signal amplification. The improvement of SNR with this method goes linearly with the number  $N$  of cavities:

$$SNR_N = N \cdot SNR_{single}$$

This technically challenging concept has for the first time been achieved in CAST-CAPP with all four cavities in a coherent data-taking mode by adjusting the frequency of the cavities within  $\pm 10$ kHz (see Figure 3 in [7]). At the same time to fulfil all the required conditions for optimum phase matching, the electrical length of the output signals, as well as the amplitude of the individual cavities, were adjusted accordingly. The phase matching concept is also important for scaled-up haloscopes a la Sikivie, e.g. the IAXO project, as it allows the coherent combination of a large number of cavities up to the order of 1000 relatively small cavities. Notably, small cavities are necessary to have resonance conditions for axions above  $\sim 10$ -20  $\mu$ eV.

The total data-taking time taken so far with phase-matching corresponds to 1543.7 hours (64.3 days) for a total frequency range of about 205.3 MHz from 5.1482 GHz to 5.3535 GHz. Combining phase-matched data as well as data from single cavities a competitive limit on the axion-photon coupling constant has been set (see Figure 2.1). The progress since the last annual SPSC meeting in October 2020 is apparent. In Figure 2.2 an extended frequency range shows the current results compared to the rest of the experiments. An overview of the analysis steps for deriving these plots is presented in Section 2.4 “Data Analysis” as well as in the supplement material in Appendix A at the end of chapter 2.

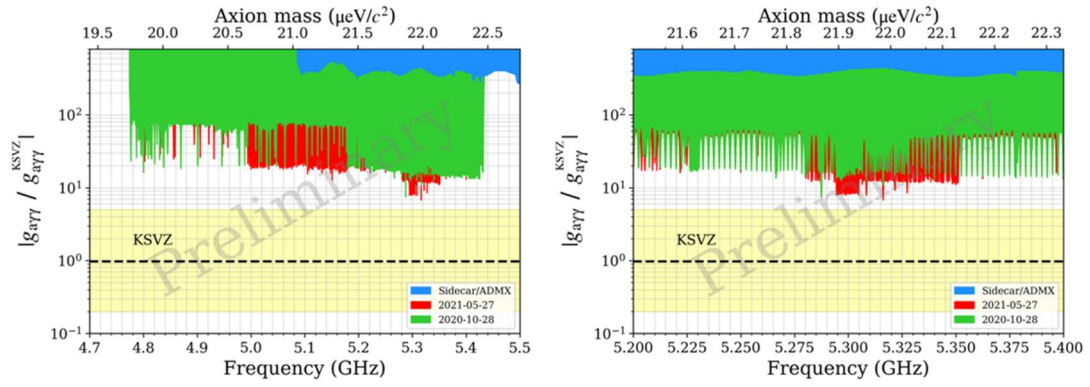


Figure 2.1: Exclusion plot comparison in the full frequency range (left) and around 5.3 GHz (right) assuming galactic halo DM axions from 10/2020 (1461 hours) and 05/2021 (3670 hours). The observed spikes correspond to longer measurement times at the specific frequencies. For comparison, the ADMX-Sidecar limit [2] is also given for galactic axions.

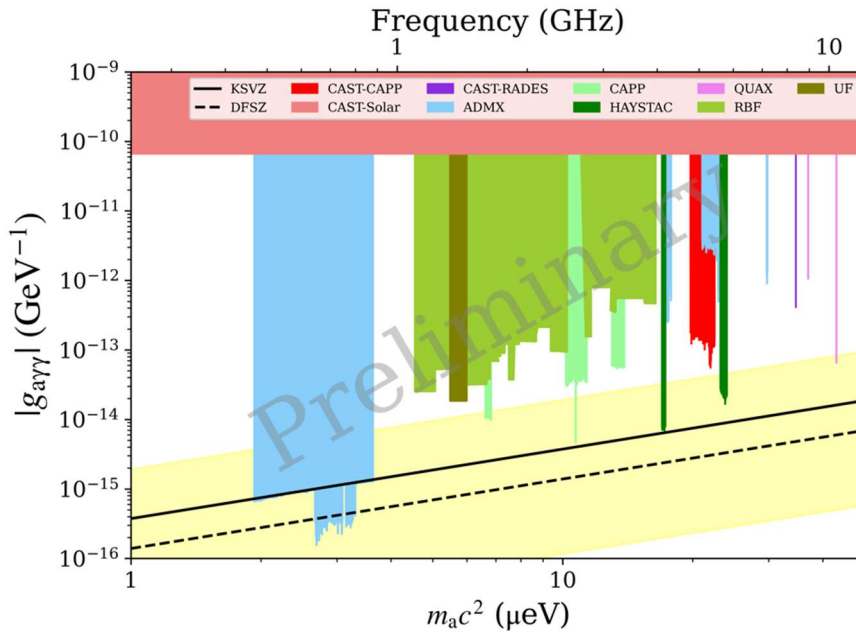


Figure 2.2: Exclusion limits by various experiments on the axion-photon coupling as a function of axion rest mass. In the red the latest CAST-CAPP results with a 90% confidence level.

## 2.3 DAQ system and strategies

### 2.3.1 DAQ chain

The whole DAQ system has been further improved considerably in both hardware (Figure 2.3) and software to provide even more functionalities for a more complete insight on the system characteristics allowing for a much faster and user-independent data acquisition procedure as well as faster daily processing and analysis.

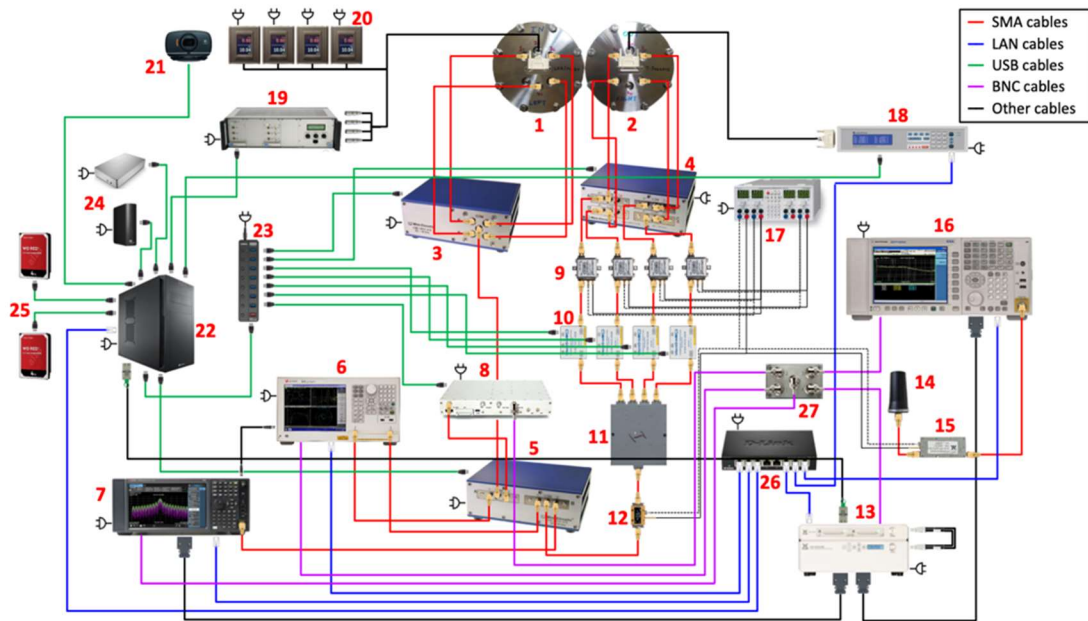


Figure 2.3: Latest CAST-CAPP hardware schematic outside-the-cryostat.

The implementation of a second measuring channel for continuous and simultaneous monitoring of ambient EMI/EMC parasites (instruments 14-16 in Figure 2.3) including all the necessary upgrades in the IQC data recorder (instrument 13) was successfully achieved (see also Section 2.3.2). The simultaneous recording from both spectrum analyzers (instruments 7 and 16) results in a doubling of the data to 3 GB per 1-min measurement. To mitigate the increased offloading, uploading to CASTOR, and processing times, a few upgrades have been performed:

- The IQC data recorder (instrument 13) storage was upgraded from **2 TB** to **4 TB** RAIDs.
- The local pc storage was upgraded from external HDD to 2 x internal SSD drives which were RAID together (instruments 25). This increased substantially the read/write speed while offloading and processing the raw data from **130 MB/s** to **940 MB/s**.
- The whole CAST network infrastructure as well as the workstation pc network card were upgraded from 1 GB/s to 10 GB/s. In practice, this increased the upload speed to the CASTOR tape system by about **5 times**.
- The multi-threading technique was implemented in processing procedures to allow for simultaneous usage of 6 / 8 cores of the local workstation PC. This allowed simultaneous processing of multiple raw data files increasing the processing speed by about **4 times**.

Additionally, a 10 MHz reference cable was connected to all new instruments through a power splitter (instrument 27) to phase lock all the various instruments and allow for higher frequency accuracy. Regarding offline tape storage, the CASTOR tape system of CERN is currently being replaced by CTA (CERN Tape Archive) system. Therefore, the migration of all the data from the old system to the new one took place in January/February 2021. All the submission scripts and the various protocols for the upload of the CAPP data to CTA through FTS were adjusted accordingly. In addition, new re-submission automatic procedures were created that allow for a direct upload of all the failed files which strongly reduces the re-submission times from about **5 hours** to **30 min**. It is noted that due to the size of the recorded files there are about 4 TB of data being uploaded daily to CTA which in turn increases the possibility of files failing. Finally, streaming of the small files below 10 MB that are uploaded on CTA through an independent protocol allows a much faster upload time for the processed and analyzed data reducing the time from **1.5 hours** to about **8 min**.



### 2.3.2 Identifying electromagnetic interferences

The observation of several unintended and intended emitters in the CAST area, operating in our frequency range initiated a wide-search operation for the identification and characterization of these frequencies. Even though the magnetic body of CAST acts as a Faraday cage shielding the cavities from outside RF leakages, a small number of strong parasites, about 30 dB above the noise floor, can make their way in the DAQ chain through outside-the-cryostat connections, amplifiers cables, etc.

Therefore, after the initial manual identification of the frequency, shape, and power of the EMI/EMC parasite signals in the CAST area, a witness channel has been installed in the DAQ chain on 18/11/2020 for automatic measurement of all these parasitic signals. This independent simultaneous measuring system performs identification of EMI/EMC parasite signals present in the CAST hall through a spectrum analyzer connected to an external omnidirectional antenna (instruments 14-16 in Figure 2.3). This works as a “veto counter” operating at the same band as the cavity measuring channel constitutes an important upgrade for signal identification which allows for an easier and faster first characterization of possible outliers (see Figure 2.4). The total exposure time since the initial installation is about 2139.9 hours (89.2 days).

It is mentioned that with the addition of this EMI/EMC measuring channel and the recent updates in the analysis procedure, the two spectra from the two simultaneously operated channels can be used to check daily for short-lived signals that could be associated to transient events. However, ambient EMI/EMC leaves similar large signatures in the cavity as transient events would do, but can be rejected on the basis of simultaneous observation outside the magnetic field (see for example Figure 2.4).

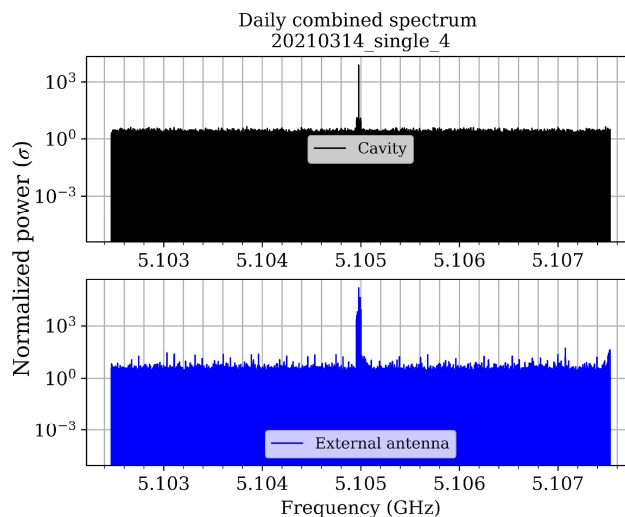


Figure 2.4: Example of an EMI/EMC parasite being present in both cavity measuring channel (upper black spectrum) and EMI/EMC measuring channel (lower blue spectrum) at the same frequency.

A significant intended emitter in the CAST hall is the 5 GHz band from WLAN coming from the Access Points located around the area. After consultation with the responsible CERN WLAN service, channels 52-56 and 116-120 interfering with our frequency band have been disabled with the achieved huge suppression being obvious around the related frequencies shown in Figure 2.5.

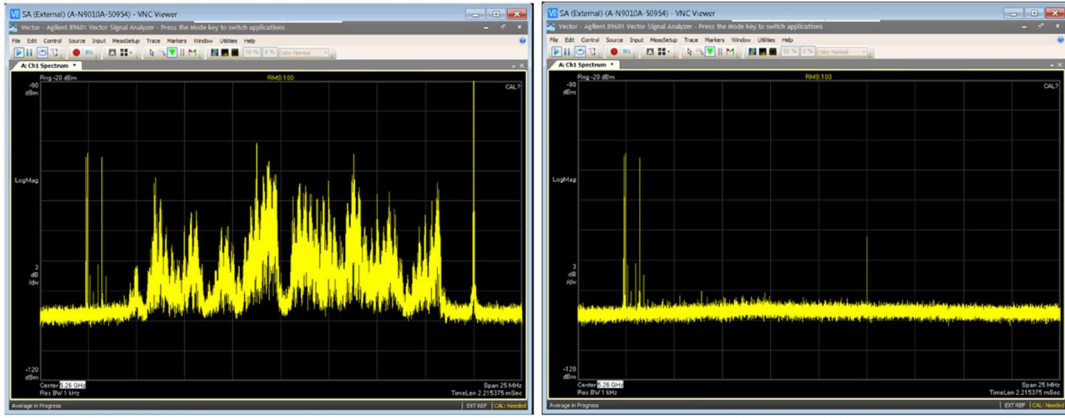


Figure 2.5: Power as a function of frequency, from 5.25 GHz to 5.29 GHz, for the 52-56 WLAN 5GHz channels emitting in the CAST area before (left) and after (right) they have been disabled.

### 2.3.3 Signal injections

Following a suggestion also by the SPSC referees, a new signal generator has been permanently installed in the DAQ chain (instrument 8 in Figure 2.3) to insert a well-defined pilot tone in the cavity measurements. This makes sure that a fake axion signal will be identified by the analysis procedure, but also provides useful information on the stability and calibration of the whole data-taking system. Recently, the implementation of an automatic signal injection procedure has been completed with a variety of signals with different amplitudes being injected, recorded, and identified by analysis in several frequencies. An example of such an injection with a 1Hz CW signal and a sweeping 5 kHz one within 10 msec is shown in Figure 2.6.

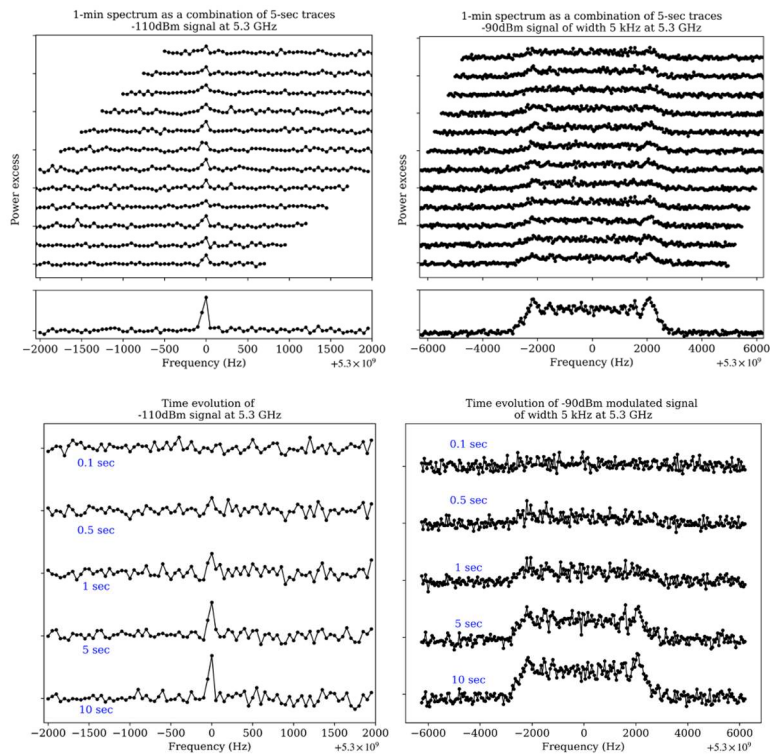


Figure 2.6: Injected signal of -110 dBm power on a cavity with a CW pulse (left column) and -90 dBm with a 5 kHz width (right column). The combination of 12 5-sec traces in a 1-min trace (upper row), as well as the time evolution (lower row), is showing the amplification of the signal as more and more data are combined, thus confirming the analysis procedure.

In addition, in a simulation an axion signal has also been generated and artificially injected into the raw data. With this simulation, the observation of such a signal via the analysis procedure is also cross-checked. In Figure 2.7 a simulated axion signal with a coupling 20 times the KSVZ limit and 7 kHz width has been recovered.

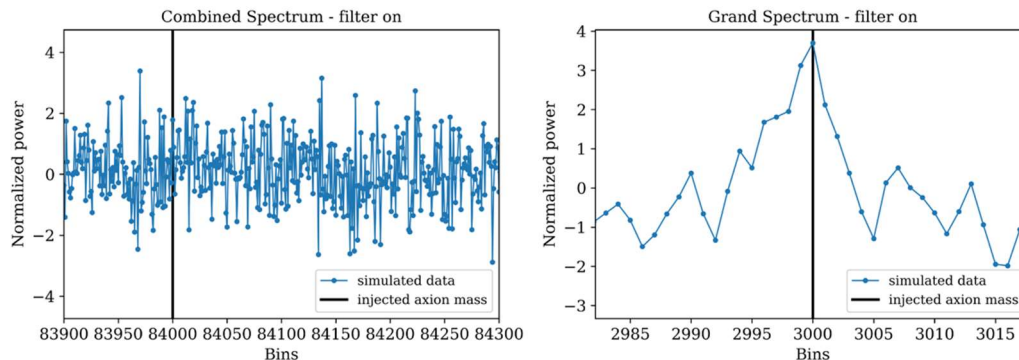


Figure 2.7: Simulation of 110-min simulated raw data including a 20 x KSVZ axion in combined (left) and grand (right) spectra. Effect of the analysis procedure is observed as a signal with higher SNR.

### 2.3.4 Fast Resonant Frequency Tuning

The design of CAST-CAPP allows to eventually profit from the transient flux enhancement [5] including gravitational self-focusing due to the density distribution of the inner Earth [6] giving rise to an eventually large circadian or peaking modulation (see Figure 1 in [7]). Therefore, in addition to the search for halo DM axions, CAST-CAPP can investigate possible axion transient events in the axion mass range  $\sim 19.7\text{-}22.4 \mu\text{eV}$  thanks to its “fast resonant scanning technique”. The CAST-CAPP cavities are tuned relatively fast to take advantage of possible streaming dark matter axions without losing sensitivity for isotropic DM halo, which was of primary interest during the data-taking period. So far, a wide axion mass range ( $\sim 660 \text{ MHz}$ ) could be scanned within a total time interval of a few hours to eventually take advantage of transient dark matter [1,5,6]. Here, the concurrent direct comparison with a simultaneously measuring second spectrum analyzer channel is in particular important to identify potential EMC/EMI noise. The analysis of the collected data towards such events is possible and will be intensified at a later stage.

## 2.4 Data Analysis

The analysis procedure has been quite improved to match the widely accepted methods followed by other experiments such as ADMX, HAYSTAC, CAPP-IBS, etc [3-4], but has also been adapted to the specific experimental conditions of CAST-CAPP. Below the most important new additions since the last SPSC annual meeting are presented along with the latest results.

### 2.4.1 Parameters optimization

The basic procedure involves the removal of the noise baseline of the processed spectra with the Savitzky-Golay (SG) filter (see Figure 2.8). SG filter is based on a moving polynomial fits of order  $p$  in window length  $W$ . These parameters,  $p$ , and  $W$ , have to be adjusted for optimal performance.

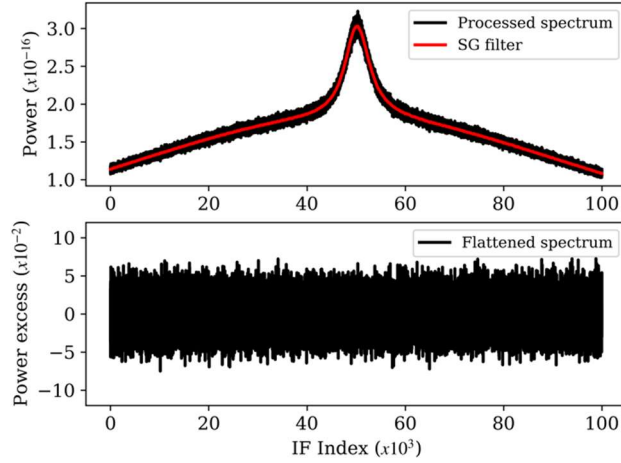


Figure 2.8: Processed spectrum and its SG filter (upper). Flattened spectrum (lower) is achieved by dividing the processed spectrum by its SG filter and subtracting 1.

SG filter is preferred by the vast majority of the axion community as a smoothing filter due to its nearly perfect pass-band. Still, the adverse effects of its imperfect stop-band should be accounted for to prevent analysis performance issues. The effect of imperfect SG filter stop-band performance on the analysis results are twofold:

- The standard deviation of the grand spectrum bin distribution is lowered by the SG filter-induced correlations among adjacent bins.
- Axion signals are attenuated due to imperfect stop-band effects.

To understand and minimize these effects, we optimize SG filter parameters  $(W, p)$  and run two simulations to quantify the two effects listed above. First, to do the parameter optimization, we investigate the transfer functions of the SG filters with varying parameters. Figure 2.9 shows the transfer functions for 2 parameter sets, namely the currently used  $W=1000, p=4$  (left) versus promising  $W=2000, p=2$  (right). Yellow (axion domain) and brown (cavity resonance domain) colored bands in the plots reflect the 2 main criteria of optimization: SG filter should have a low transmission for axion signal and high transmission for cavity resonance bump. We see that a change of parameters from  $(W, p) = (1000, 4)$  to  $(2000, 2)$  brings -3 dB point of the filter closer to cavity resonance domain keeping its transmission at constant 0 dB (maximum) and lowers the axion signal transmission from  $\sim 20$  dB to  $\sim 30$  dB fulfilling our criteria. We are currently running a new analysis campaign to apply a new SG filter with these optimized parameters.

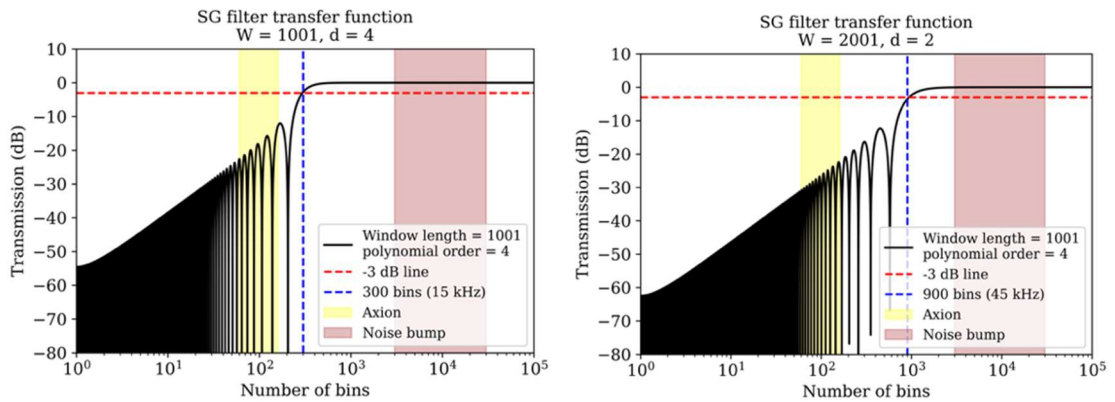


Figure 2.9: Different parameters of SG filter to maximize the noise bump transmission while minimizing the axion transmission. SG filter transfer function for parameters  $(W, p) = (1000, 4)$  is shown on the left, and  $(W, p) = (2000, 2)$  on the right.

We selected the promising parameters  $(W,p)=(2000,2)$  by investigating the SG transmission as a function of  $W$  for several integer  $p$  values as depicted in Figure 2.10. There we selected the  $(W,p)$  point that maximizes cavity transmission (dashed lines) and minimizes the axion transmission (solid lines).

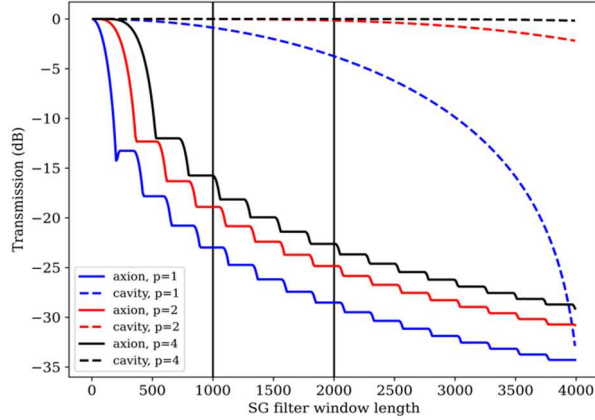


Figure 2.10: Variation of cavity (solid lines) versus noise bump (dashed lines) transmissions as a function of SG fit-window length,  $W$ , and for several integer polynomial orders,  $p$ .

The first of the two simulations is used to quantify the SG filter induced standard deviation reduction in the grand spectrum. In this simulation, we run 104 experiments, each with 100 simulated processed spectra made of random noise added on sample noise baselines. We evaluate the covariance of the nearby bins using the mean of the covariance distributions for  $n$  cases where the bin displacement is varied from 1 to  $n-1$  where  $n$  is equal to 28 and 5 for the rebinned and the grand spectra, respectively. Figure 2.11 shows the results of the simulation for the grand spectrum where the covariance of the nearby bins is quantified to be  $-0.0995$ ,  $-0.0973$ ,  $-0.0923$ ,  $-0.0835$  with  $\pm 0.0002$  uncertainty as bin spacing is varied from 1 (bins that are just next to each other) to 4. The behavior of decreasing covariance is expected as the bin spacing increases. To test the null hypothesis, we conducted the same simulation on random noise spectra with a flat baseline without SG filter application and we observed no correlations among adjacent bins as expected.

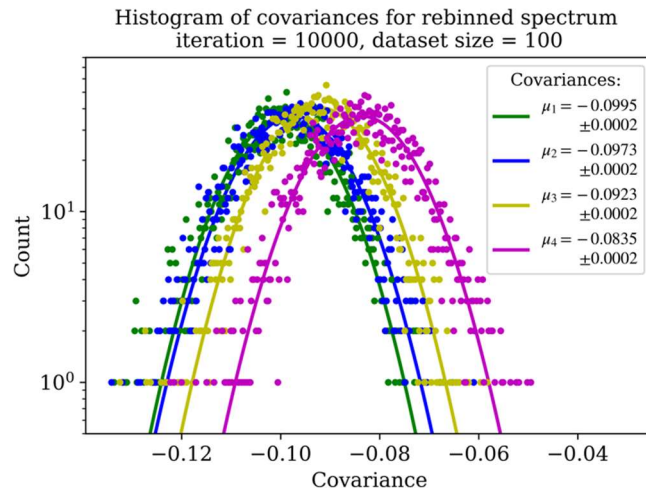


Figure 2.11: Results of the simulation to quantify adjacent bin correlations in the grand spectrum due to imperfect stop-band of SG filter.

The analysis with  $(W,p)=(1000,4)$  results in a grand spectrum with standard deviation  $\sigma=0.74$  due to SG filter complications where the expected number is 1. We use the results of the simulation above in a feedback loop to correct the weights used in the analysis and the corrected standard deviation  $\sigma=0.96$ , much closer to our expectation of 1. First indications of the currently undergoing analysis with  $(W,p)=(2000,2)$  show we can achieve  $\sigma\sim 1$  after the correction.



The second of the two simulations aims to quantify axion signal attenuation due to imperfect SG filter stop-band. We simulate  $10^3$  experiments with injections of digitally synthetic axion signals in 100 simulated spectra. After analyzing each experiment, we histogram the amplitude of axion signal carrying bins and compare the results for the cases where SG is used or not used. Results of this simulation indicate that a prospective axion signal SNR may be attenuated up to  $\sim 50\%$  given the SG filter parameters  $(W,p)=(1000,4)$  meaning an attenuation coefficient of  $\eta=0.5$ . Since the exclusion performance is proportional to the square root of the SNR, the  $\eta=0.5$  value indicates a decrease in exclusion by factor  $\sim 0.7$ . Figure 2.12 shows the histograms of the axion signal carrying simulated bins resulting from 2 channels of the simulation: with (right) and without (left) SG filter application.

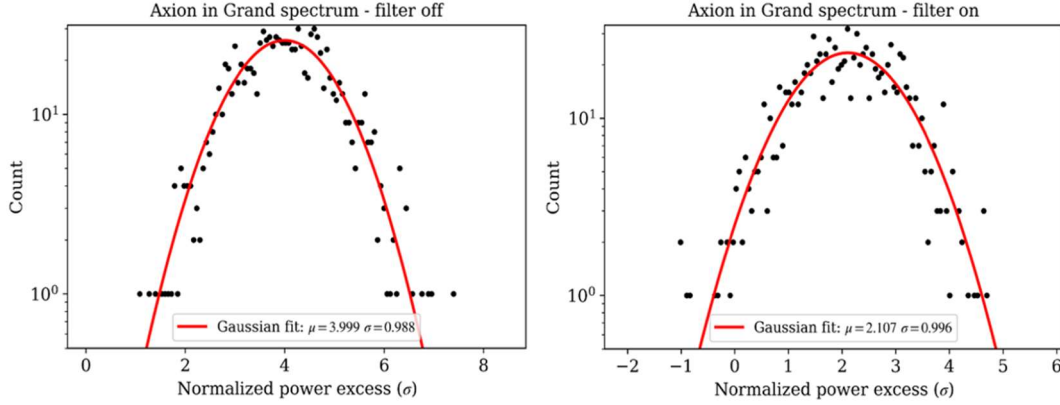


Figure 2.12: Simulated axion power with (right) and without (left) SG filter.

ADMX and HAYSTAC report  $\eta$  ranging between 0.7-0.9 meaning they can preserve 70% - 90% of the axion signal. This shows we have room for improvement here as well. First indications of the currently undergoing analysis with  $(W,p) = (2000,2)$  SG parameters show that  $\eta$  will increase to the region where our competitor experiments operate meaning that we will preserve the SNR of an axion signal better.

#### 2.4.2 Noise distribution cross-checks

An important check in the quality of the receiver chain is to observe the expected noise properties. In this case, we want to observe the distribution features of the Johnson-Nyquist (thermal) noise in our spectra. Many noise distribution histograms that we showed to SPSC so far displayed Gaussian distribution (that look like a parabola on a logarithmic scale) as dictated by the central limit theorem due to the massive averaging of many spectra. So, to distinguish the noise characteristics, we should focus on the non-averaged spectrum. The left plot in Figure 2.13 shows voltage and power distributions of a raw spectrum aligned well with theoretical expectations of  $\chi$  and  $\chi^2$  of 2 degrees of freedom, respectively. We tested the well-known  $1/\sqrt{N}$  factor that explains the decreasing error of the mean as more and more spectra are averaged. As the right plot of Figure 2.14 shows, we observe the expected relation: As the data integration time is increasing, the standard deviation of the bins in the averaged spectrum decrease with factor  $1/\sqrt{\delta v t} \equiv 1/\sqrt{N}$ .

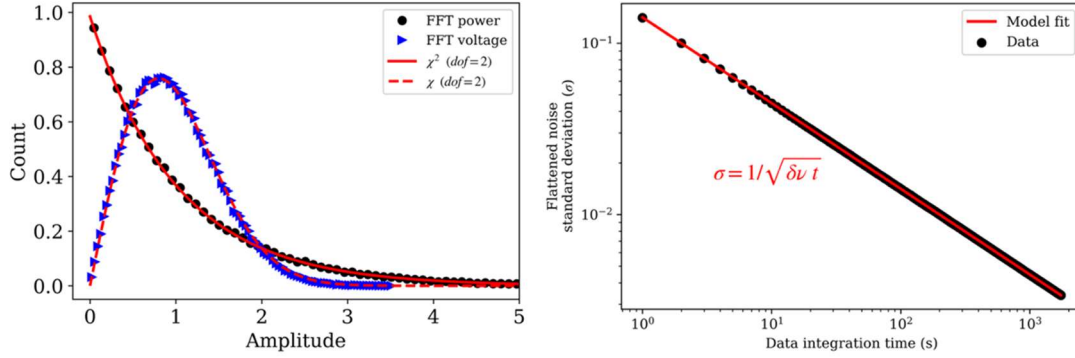


Figure 2.13: Voltage and power distributions of non-averaged raw spectra (left) and the variation of the averaged spectrum standard deviation as a function of averaging time (right).

### 2.4.3 Quality checks

The first important part of the CAST-CAPP analysis procedure is a series of quality checks on the processed spectra. The selection criteria of Table 1 are applied on each 1-min data chunk and those data which do not pass this selection are not considered in any further analysis step. These criteria verify that unwanted effects such as mechanical vibrations, which influence the frequency, amplitude, and the Q-factor of the resonance as measured in transmission through the VNA (instrument 6 in Figure 2.3) before and after each 1-min measurement, are rejected.

More specifically criteria 1-4 from Table 1 concern all measurements, both with single and phase-matched cavities, while criteria 5-8 are applied only for the phase-matched data sets. It is noted that the various limits are conservative. As an example, the theoretically calculated mismatch between the frequencies of the phase-matched cavities is about 100 kHz for our setup, while our limit is set to 20 kHz in the transmission measurement taking place before the 1-min recording and 80 kHz in the measurement taking place at the end of the 1-min recording.

Table 1: Selection criteria for 1-min processed data files.

Nr.	Parameters	Criteria
1	Frequency stability	$\Delta\nu_0 < 100$ kHz
2	Amplitude variation	$\Delta A_0 < 3$ dB
3	Quality factor	$10^3 < Q < 4 \times 10^4$
4	Quality factor shift	$\Delta Q < 7 \times 10^3$
5	Frequency mismatch	$< 20$ kHz (before)
6	Frequency mismatch	$< 80$ kHz (after)
7	Amplitude mismatch	$< 1$ dB
8	Temperature mismatch	$< 3$ K

For B=ON data the total number of processed 1-min files is 233311, from which 11592 of them did not pass the quality checks ( $\sim 4.97\%$ ). The corresponding disqualified data for B=OFF is 461 out of 24138 ( $\sim 1.9\%$ ).

### 2.4.4 Results and outliers

The grand spectrum as well as its histogram of the latest B=ON data is presented in Figure 2.14. The target SNR for an axion signal that is likely to be detected is 5 with the confidence level set to 90%. This results in a threshold of  $3.72\sigma$  on the grand spectrum bins for them to be flagged as outliers.

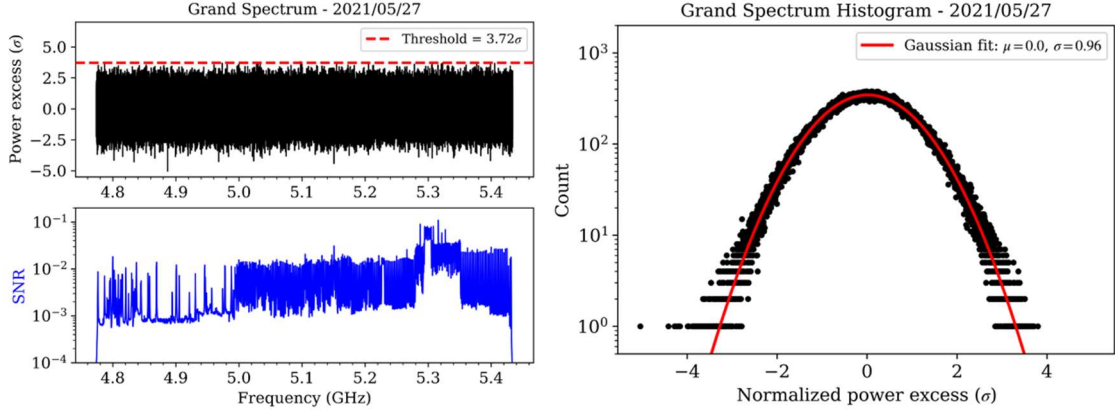


Figure 2.14: Grand spectrum (left) and its histogram (right).

The latest analysis results for the B=ON data with the confidence level set to 90% contained in total 60 outliers being above our defined threshold of  $3.72\sigma$ . 11 of them were identified as fake signal injections, while 9 of them were verified as EMI/EMC parasites through the second EMI/EMC measuring channel described in Section 1.2.1. The remaining 40 outliers were identified as statistical outliers which agree with the theoretical expectation of  $\sim 47$  grand spectrum bins exceeding the threshold. A rescan procedure has been initiated for these 40 outliers excluding them successfully all based on the following procedure:

1. The outlier signals should have the correct axion characteristics to be marked by the analysis procedure as promising ones. The expected dark matter halo axion signal width should be about 5-7 kHz.
2. There should be no observable parasite in the data from the simultaneously measuring EMI/EMC channel.
3. The measured outlier signal should be persistent in time and increase in amplitude while the rescan procedure is taking place.
4. A rescan with the same and different cavity(ies) configuration should not change the resulting signal. If it does then it should be related to a cavity-dependent RF noise.
5. Switching to a resonant mode that does not couple to axions should “kill” the signal.
6. Switching B=OFF as well as changing the B field to intermediate values (between 0 and 9 T) should have the corresponding effect on the outlier based on the theoretically expected magnetic field dependence.

Therefore, since no outlier has survived the aforementioned elimination procedure, the exclusion plot of Figure 2.1 and Figure 2.2 could be calculated.

## 2.5 Future Prospects

Scanning of the whole parameter space ( $\sim 4.8$  GHz – 5.4 GHz) with all 4 cavities (single and phase-matched) in order to improve the sensitivity for dark matter axions will be performed if CAST is granted more data taking time. The prospects for 6 and 12 months of data-taking are shown in Figure 2.15.



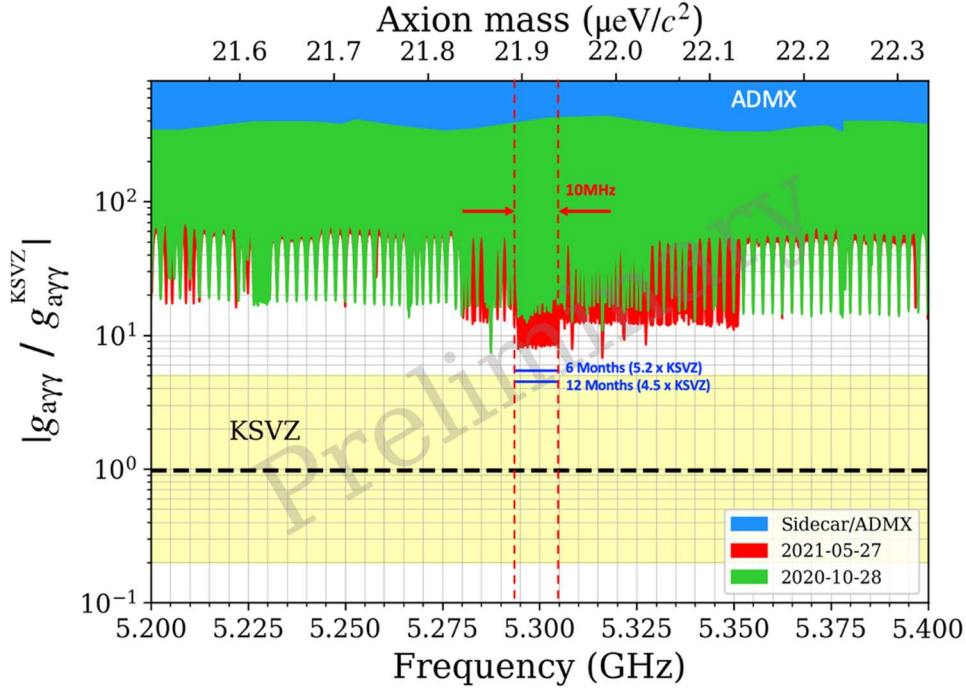


Figure 2.15: Projected relic axion detection sensitivity (red-dashed line) following 6 and 12 more months of data taking.

The CAST-CAPP sub-detector also has the following possibilities based on a series of short interventions:

- The existing tuning mechanism can be adjusted, providing a shift of the current 660MHz scanned frequency range. The total achievable range is about 1 GHz. This intervention would aim to extend the sensitivity of CAST-CAPP cavities to new and unexplored axion mass ranges towards lower and higher values.
- The tuning springs and/or the piezoelectric motors can be upgraded following a suggestion by the manufacturing company for a smooth and even faster tuning with less heat dissipation extending the current tuning range by about 100 MHz ( $\sim 4.7$  GHz – 5.5 GHz) and allowing a search for even shorter transient events. Though, a complete replacement of the piezoelectric motors has about 3-4 months delivery time including implementation and testing.
- The cryo-contact of cavities 1-3 with the magnet bore, can be improved allowing for an even lower temperature (by about 4 K) and therefore a higher sensitivity.
- Improvement of the quality factor  $Q$  of the present cavities up to  $\sim 10^6$ , covering with HTS YBCO tape their inner surface. This is a project and could be considered in 2022 depending on the achieved results until then.
- The duration of a real signature is one important parameter for the streaming-DM scenario. Hence, simulation work on cosmological axion streams which take into account solar system bodies is in progress with external collaborators with high expertise in the field.

## 2.6 Concluding Remark

With the data taken so far in CAST, we have already demonstrated a promising sensitivity to axions with the CAST-CAPP cavities. We continue upgrading the experiment while aiming to understand the background from thermal noise and ambient EMI, which will further expand the reach of CAST into new axion parameter space and position CAST in the DM axion field. This challenging question CAST wants to answer in full and not leave it to the competitors. Finally, envisioning continued operation for an estimated data-taking time of 12 months we could reach into the theoretical band in the mass range around 5.3 GHz as indicated in Figure 2.15.

## References

- [1] S.G. Turyshev, Phys. Rev. D **95**, (2017) 084041.  
SG Turyshev, V.T.Toth, Phys. Rev. D **96**, (2017) 024008.
- [2] C. Boutan (ADMX Collaboration), Phys. Rev. Lett. **121**, (2018) 261302.
- [3] S. Ahn et al., J. High Energ. Phys. **2021**, (2021) 297
- [4] Brubaker et al., Phys. Rev. D **96**, (2017) 123008.
- [5] H. Fischer, X. Liang, Y. Semertzidis, A. Zhitnitsky, K. Zioutas,  
Phys. Rev. D **98**, (2018) 043013 and references therein.
- [6] Y. Sofue, Galaxies **2020** 8(2), **42**, (2020).
- [7] SPSC Report 13/10/2020; <http://cds.cern.ch/record/2738387>

## APPENDIX A: Overview of the analysis procedure

Data is recorded as 1-minute-long voltage readings in binary format. Each file has  $\sim 1.5$  GB size per recording channel. These data files are divided into chunks of length  $1 / 50 \text{ Hz} = 20$  milliseconds where 50 Hz will be the resolution bandwidth of the combined spectrum. Data is converted to the frequency domain by applying Fast Fourier Transform (FFT) on individual chunks. Then 3000 FFT chunks belonging to a single data file is combined to obtain the processed spectrum. Processed spectra are saved in the local PC. Figure A1 shows the effect of averaging FFT spectra.

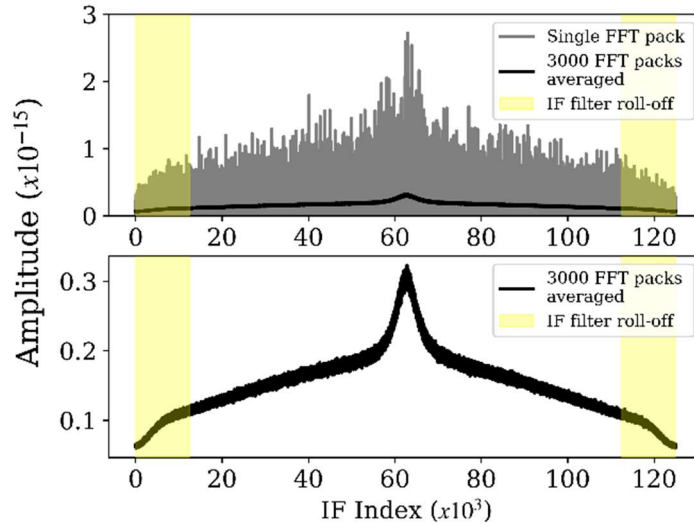


Figure A1: Averaging 3000 FFT spectra to obtain a processed spectrum.

Data analysis starts with the quality check on processed spectra. Auxiliary data (e.g., the cavity resonance frequency before and after each measurement) recorded by VNA determine if an individual processed spectrum should be involved in the analysis or not (e.g., center frequency shift due to vibrations of the cavity during a single measurement should be smaller than 100 kHz). Table 1 gives a detailed account of these qualification criteria. Processed spectra are flattened to smooth out the cavity noise bump due to resonance mode. Figure 2.8 shows Savitzky Golay (SG) filter (red) applied to the processed spectrum. The processed spectrum is divided by its SG filter and then 1 is subtracted to have a flattened spectrum of mean = 0 and standard deviation =  $1/\sqrt{\delta\nu t}$  where  $\delta\nu$  is the resolution bandwidth = 50 Hz, and  $t$  is the integration time = 1 min.

Flattened spectra are scanned for possible IF (intermediate frequency) parasite signals. First, all flattened spectra are divided into 3 groups and each group is averaged within itself. IF parasitic spectrum bins in these averages stand out as unexpectedly high amplitude spikes. If such a bin exists in at least

2 of the 3 averaged groups, that bin is labelled as IF parasite and discarded from the rest of the analysis procedure. Figure A2 shows 2 IF parasites that are discarded.

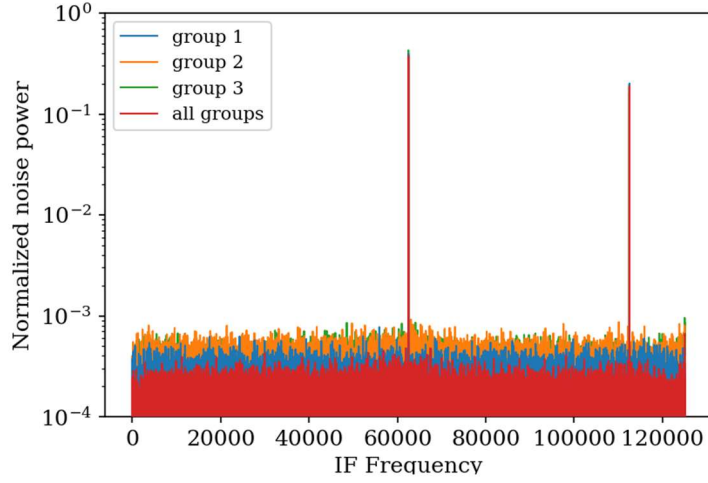


Figure A2: Intermediate frequency contamination check. 2 peaks are labelled and discarded as IF parasites.

Flattened spectra are scaled according to the noise parameters such as Boltzmann constant,  $k_B$  and the system noise temperature,  $T_s$ , and the axion signal power which varies across the spectrum, having a maximum at the center of the spectrum on the cavity resonance.

$$p_{ij}^S = \frac{k_B T_{s,j} \delta\nu}{P_{Axion,ij}} p_{ij}^F$$

$$\sigma_{ij}^S = \frac{k_B T_{s,j} \delta\nu}{P_{Axion,ij}} \sigma_{ij}^F$$

Here index  $i$  iterates over flattened spectra whereas  $j$  denotes bins in a spectrum. This scaling ensures the SNR of an axion power carrying bin to be equal to the theoretical model.

$$\text{SNR} = \frac{P_S}{\sigma_{noise}} = \frac{P_S}{k_B T_S} \sqrt{\frac{t}{\Delta\nu}}$$

The scaled spectra are then combined with weighted averaging optimized by the maximum likelihood (ML) principle.

$$p_k^C = \sum_{j=1}^{m_k} w_{kj} p_{kj}^S$$

$$\sigma_k^C = \sqrt{\sum_{j=1}^{m_k} w_{kj}^2 (\sigma_{kj}^S)^2}$$

$$w_{kj} = \frac{(\sigma_{kj}^S)^{-2}}{\sum_{j=1}^{m_k} (\sigma_{kj}^S)^{-2}}$$

where index  $k$  iterates over the scaled spectrum bins  $j$  that correspond to the  $k^{\text{th}}$  RF bin of the combined spectrum. Lastly, the combined spectrum bins are normalized.

$$x_k^C = p_k^C / \sigma_k^C$$

$$\text{SNR} = (\sigma_k^C)^{-1}$$

Figure A3 illustrates the procedure that leads to the combined spectrum. Figure A3-upper shows the scaled spectra aligned according to the RF axis. Figure A3-middle shows the combination of the scaled spectra with weighted averaging. Figure A3-lower shows the normalization of the combined spectrum.

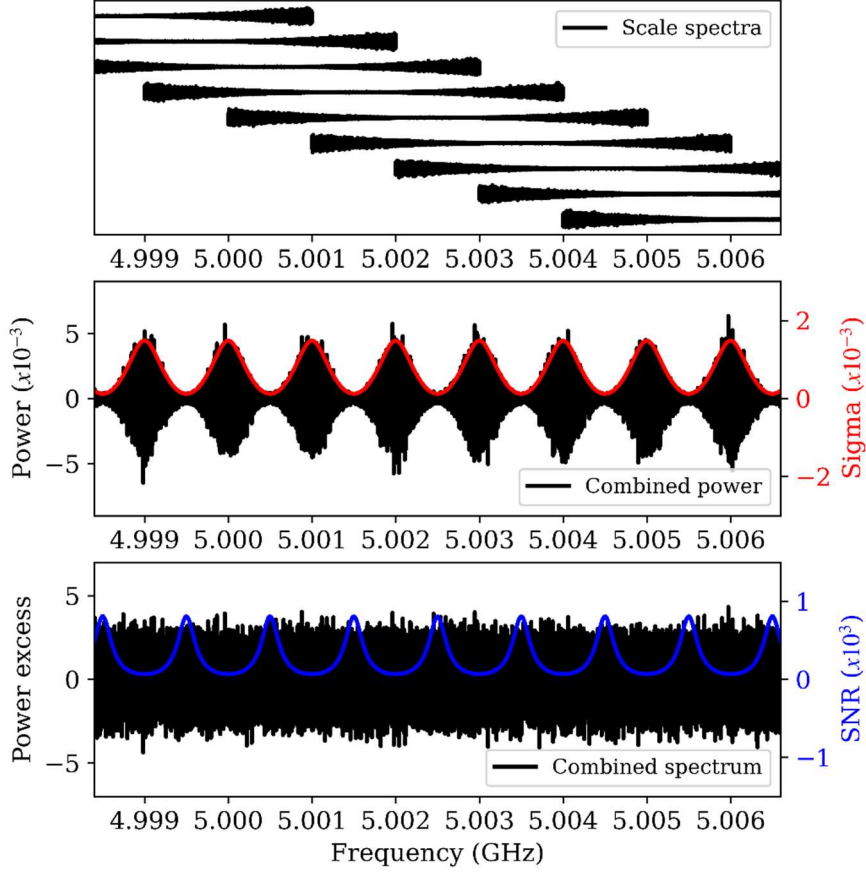


Figure A3: Generation of the combined spectrum.

The combined spectrum is rebinned (the number of bins is decreased by a factor of 1/28) with ML weights consistent with the expected distribution of the axion signal. Rebinned spectrum is scaled and transformed into the grand spectrum by taking convolution with the expected axion signal shape in the lab frame (Figure A4).

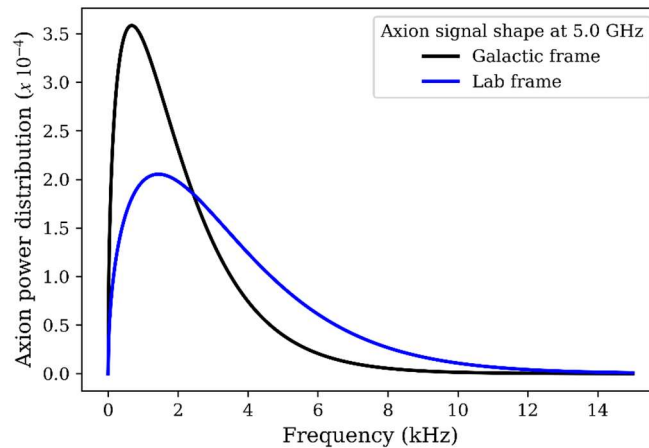


Figure A4 Axion line shape.

We convolve axion line shape over a  $K_g=5$ -bin boxes of the grand spectrum using  $L_q$ ,  $q=0,1,2,3,4$ .

$$L_q = K_g \int_{\nu_a + q\delta\nu_r}^{\nu_a + (q+1)\delta\nu_r} f_{Lab}(\nu) d\nu$$

$$p_g^G = \sum_{r=g, q=0}^{q=K_g-1} w_{r+q} p_{r+q}^R / L_q$$

$$w_{r+q} \approx \frac{(\sigma_{r+q}^R / L_q)^{-2}}{\sum_{q=0}^{K_g-1} (\sigma_{r+q}^R / L_q)^{-2}}$$

$$(\sigma_g^G)^2 = \sum_{r=g, q=0}^{q=K_g-1} \left( w_{r+q}^2 (\sigma_{r+q}^R)^2 + 2 \sum_{q'=0}^{q-1} w_{r+q} w_{r+q'} \text{COV}(p_{r+q}^R, p_{r+q'}^R) \right)$$

Here,  $r$  and  $g$  are RF indices of the rebinned and the grand spectra, respectively. Covariance terms at the end of the last equation are calculated by Monte-Carlo simulations. Figure 2.14 shows the resulting normalized grand spectrum and its histogram.

As next, we perform hypothesis testing steps on the grand spectrum to find a prospective bin that deposits axion power. We set target SNR=5 and confidence level=90% for candidate selection which leads to threshold = 3.72 (see Figure A5).

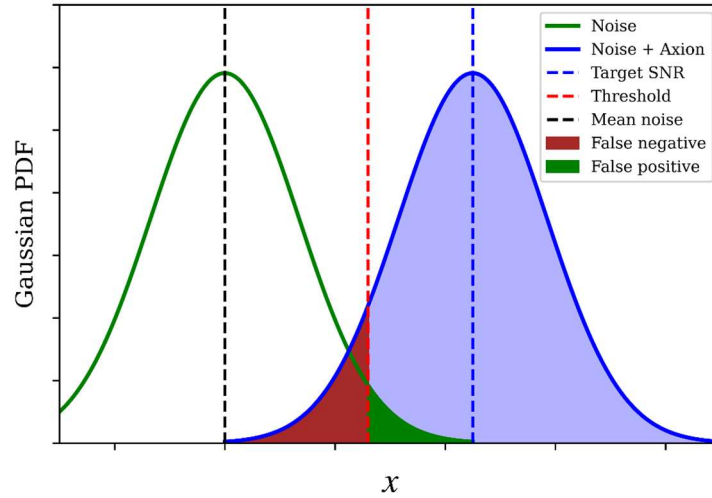


Figure A5: Hypothesis testing.

We label the grand spectrum bins that exceed this threshold as rescan candidates. We had in total 60 rescan outliers that passed the threshold. With the help of the 2<sup>nd</sup> channel external antenna, we spotted 9 outliers as EMI/EMC and removed them from our analysis pipeline. We also identified 11 outliers resulting from fake signal injections in the grand spectrum. The remaining 40 more outliers were proven to result from statistical fluctuations as all of them averaged out after rescanning. As none of the candidates survived the scrutiny, we prepared an exclusion plot using relation

$$|g_\gamma^{min}|_g = \sqrt{\frac{\text{SNR}_T}{(\sigma_g^G)^{-1}}} |g_\gamma^{KSVZ}|$$

The resulting exclusion plot is given in Figure 2.1 and Figure 2.2.



## Other sub-projects

### 3 RADES – High-mass axion search

#### 3.1 Developments since October 2020

##### 3.1.1 Submission of 2018 data-taking results for publication

In the last report we mentioned working on the finalization of the 2018 data-analysis. Between October and April, we worked on several fine details of the analysis such as the impact of the filtering procedure on a potential axion signal, which we now think has been addressed in a correct fashion. Consequently, after a collaboration-internal review, the results of the 2018 data-taking campaign of the CAST-RADES sub detector have been submitted to the arXiv and can be found at <https://arxiv.org/abs/2104.13798> and subsequently to JHEP. For convenience, we show in Figure 3.1 the resulting exclusion limit. The reported results constitute one of the most sensitive high-mass axion searches, only superseded by a QUAX result recorded at much lower temperatures.

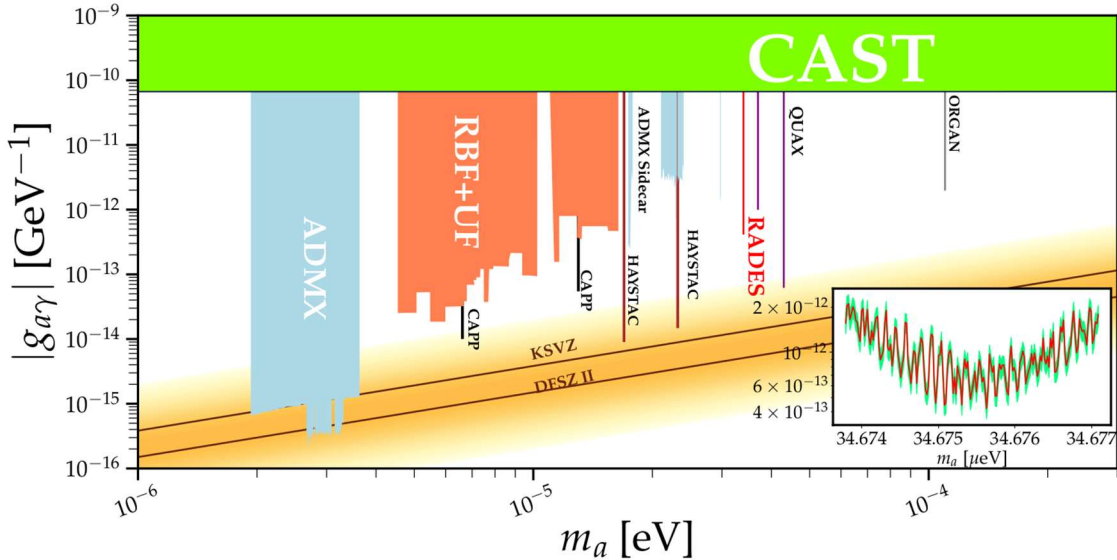


Figure 3.1: Axion-photon coupling vs axion mass phase-space. In dark red the CAST-RADES axion-photon coupling exclusion limit with 95% credibility level presented in this manuscript. The coupling-mass plane is shown in natural units for consistency with most literature in the field. Inset: Zoom-in of the parameter range probed in this work ( $34.6738 \mu\text{eV} < m_a < 34.6771 \mu\text{eV}$ ), where the green region represent the uncertainty of the measurement.

##### 3.1.2 Data-taking 2020-2021

The stability problem mentioned in our last report (<https://cds.cern.ch/record/2738387/files/SPSC-SR-277.pdf>) was resolved in October 2020. We were able to trace it back to a loose cable connection at the upper part of the magnet which cannot be always accessed. Upon repair, the set-up displayed satisfactory quality and we were able to take around 15 days of good data in 2020, with the limitations explained in the previous report related to the small Q0. Unfortunately, it seems that after the cooling of the magnet in the beginning of 2021, another obstacle occurred. Figure 3.2 below shows the 30 cavity resonances on different dates with (left) and without (right) passing the signal through the cryogenic LNA. We are able to switch between these two options using a cryogenic switch. As can be seen, a problem is present in the data of February 1<sup>st</sup> (in blue) using the line with the LNA in the sense that the cavity structure is not visible anymore (contrary to measurements from 2020 in green and orange). The fact that the cavity is visible on the line without the LNA indicates that the problem



doesn't originate from the cavity itself. Through a set of measurements we can also almost certainly exclude a problem with the LNA itself. The most likely explanation for our findings is a problem in the cryogenic part of the magnet connecting the LNA with the cavity. Since the amplification of the LNA is needed to observe a potential axion signal, the current status of our set-up is insufficient for useful physics data. Repair is also impossible without an intervention, which would have stopped the CAPP data taking for several weeks and thus was not requested.

From the current run we are thus left with 15 useful days of data from 2020 which will be analysed. Priority until now however was in finishing the 2018 analysis, which has been achieved (see above).

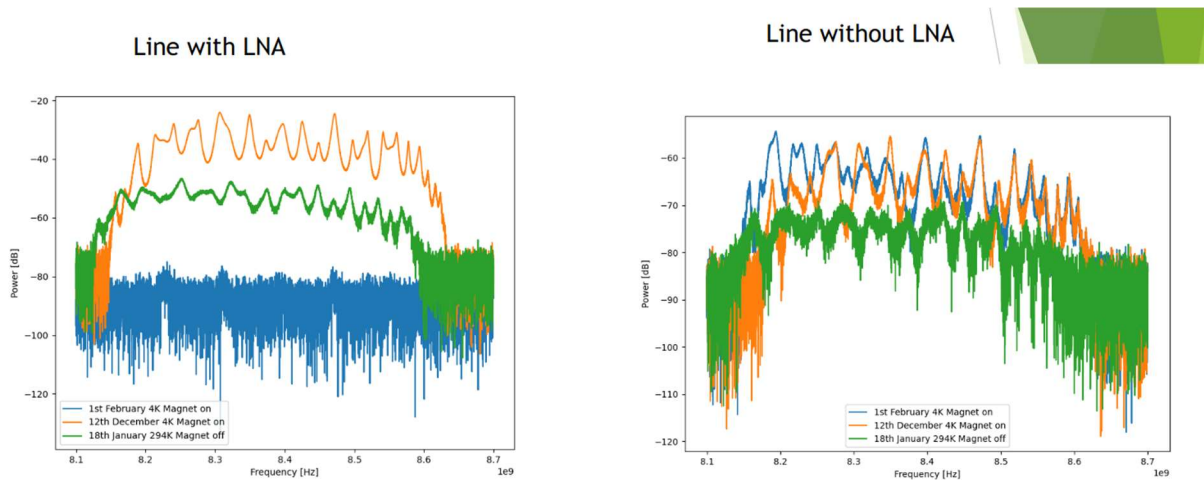


Figure 3.2: Cavity resonances on different dates with (left) and without (right) passing the signal through the cryogenic LNA.

### 3.2 Future possibilities for RADES in CAST

In the event of a continuation of data-taking with CAST, our group's aim would be to install a setup promising good physics results avoiding as much as possible the risk of another loss of data. Thus, even though we have demonstrated the tunability of our cavities in cryogenic environments, we would be reluctant of a fast installation of a tunable cavity. The reason is that the demonstration of tunability was performed for manual tuning and a cryogenic motor has not been included in our tests yet.

We have avenues to improve the unloaded quality factor of the currently installed cavity, by removing and possibly brazing the cavity. The poor unloaded quality factor was at the heart of many issues, before the cable connection was lost. In case we have on the order of 2-3 months between CAST reopening and renewed data-taking, such an attempt can well be undertaken and, if successful, could be expected to yield a good physics result as already proven on 2018 data. In parallel, several R&D developments for a future data campaign in babyIAXO are ongoing.

## 4 The new solar axion data taking campaign with the IAXO pathfinder system at CAST

### 4.1 Summary and goals

Solar axion searches were resumed at the sunrise end of CAST detector with the IAXO pathfinder system, composed by the X-ray optics and an improved, low background and low threshold gaseous detector. The goal of the current data taking campaign is to:

1. Improve the result obtained in the 2013-15 phase on  $g_{a\gamma}$ .



2. Clarify the statistical/systematic origin of the  $2\sigma$ -excess observed in the sunrise Micromegas (SRMM) data set.
3. Get insight into the limitations of current detection parameters (background and threshold) in microbulk technology.
4. Provide technical and operational experience for the future BabyIAXO and IAXO.

## 4.2 Preliminary considerations

The last vacuum solar axion data-taking campaign of 2013-15 was a success, providing the best limit so far on  $g_{a\gamma}$  by CAST. The effective background level (number of background counts expected in the energy- and focal-area-region of interest) is of about 1 count per 6 months of operation of the experiment ( $\sim 0.003$  counts/hour). However, the relatively low statistics collected with this system in the 2013-15 campaign (290 tracking hours) makes the result statistics-limited, which partially hinders its impact in the overall limit.

The current understanding of the background limitations of microbulk detectors allow to devise a number of steps to carry out in the search for even lower background levels. The opportunity of operating these improved systems at CAST offers a realistic environment to validate such improvements, specifically the usage of Xe-based gas mixtures.

## 4.3 Status and achievements

The present data taking has already provided additional statistics at CAST with the mentioned system, doubling the tracking hours. During the Ar+2.3% isobutane phase (2019-2020) we collected 3030 hours of background, including 152 hours of tracking time, and in the current Xe-based mixture phase (2020-2021) we have 3425 hours of background including 132 hours of tracking time (as of 17/05/2021). The preliminary analysis shows that the background rate is at the level of  $\sim 10^{-6}$  c/keV/cm<sup>2</sup>/s, compatible with the previous result, as it was published in 2017 (Nature Phys. 13 (2017) 584-590).

## 4.4 Data taking campaign with Xe-based mixtures

We started data taking with a new Xe-based gas mixture, in particular 48.85% Xe + 48.85% Ne + 2.3% Isobutane, in September 2020, after a gas system upgrade to allow for recirculation. The system works and data have been taken successfully, which is an important technical achievement. The energy spectrum is free of the 3 keV Ar escape peak and is thus expected to reduce the background in this energy region. This was an important milestone as the peak of Primakoff produced axion is expected in that energy.

During data taking in recirculation conditions, we have observed a gain loss with time (Figure 4.1). After replacing the gas filters and injecting new gas several times, the effect was still present. The current hypothesis is that permeation of the different gases in the mixture through the window is different. Isobutane is the biggest molecule among the three, so its relative amount in the mixture increases. The increase in quencher leads to a lower gain for a given voltage.

The energy threshold is affected by the gain, ranging between 0.8 keV for the higher gain runs and 3 keV for the lower gain runs.

The 25<sup>th</sup> of March 2021, while a gas injection procedure was being performed, the gas in the bottle was accidentally lost. We now have a limited amount of gas ( $\sim 15$  l), but the system has been adapted to the new situation and the response is being satisfactory.

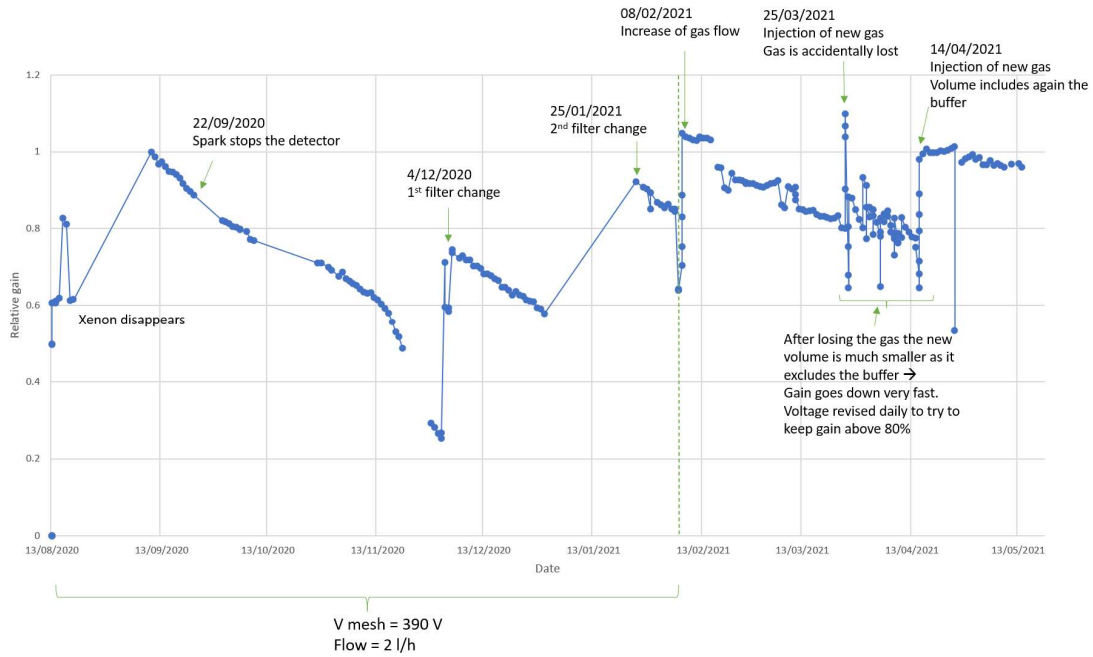


Figure 4.1: Relative gain computed as the 5.9 keV peak position in each of the daily calibration runs. Relevant interventions or changes in the conditions are annotated.

We found that the conditions and voltages that are required to work with the current Xe-based gas mixture are pushing the detector to the limit. The current in the mesh shows many spikes, some of which end up causing trips and occasionally sparks. Some of these sparks have broken channels in the readout and they had to be disconnected. One of the disconnected channels is close to the centre of the readout and it will have to be handled carefully during the analysis (Figure 4.2).

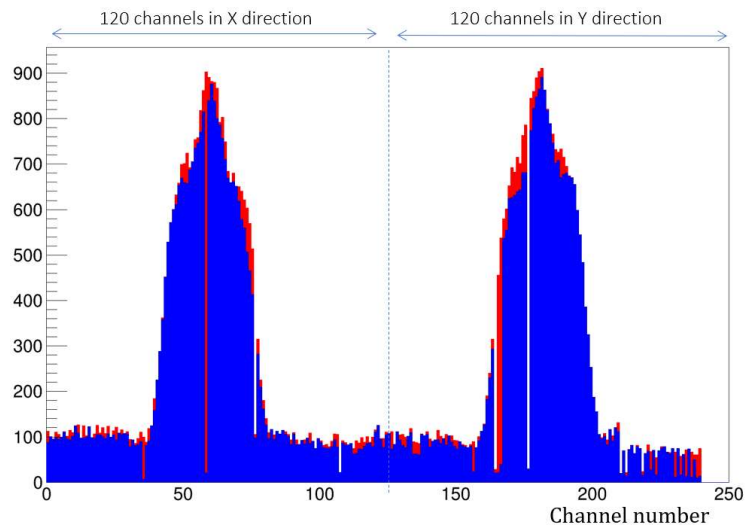


Figure 4.2: Readout channel activity histogram for calibration runs, where signal is focalized in the centre of the readout. In red, a run taken before disconnecting one of the central channels and over imposed in blue, one of the latest runs. The red channels that can be seen are those that have been lost during the data taking period.

## 4.5 Data analysis

A new public release of the software has been published, including all the developments made during the last year specifically for CAST: <https://github.com/rest-for-physics>.

Some of these improvements include new ways of computing the size of the event in the readout XY plane to better match what we see. The study of the second track has also been implemented, as in the current setup in which we save all the channels instead of only those that are above a given threshold, we see larger events that many times have more than 1 track. Finally, some noise reduction strategies are also being tested, which may lead us to reach an even lower energy threshold. The full datasets, both with Ar and Xe, will be re-analyzed once all the improvements are totally implemented and well tested.

#### 4.6 Preliminary background spectrum with Xenon

A very preliminary background level including only 1 track events and applying cuts based on  $^{55}\text{Fe}$  calibrations with Xenon has been computed, pointing towards levels of a few  $10^{-6}$  c/keV/cm<sup>2</sup>/s. As seen in Figure 4.3, the argon fluorescence peak at 3 keV no longer appears, reducing the background level in that range. The somehow larger background above 4 keV is attributed still to imperfections in the preliminary calibration. The final Xe analysis must wait until the end of the data taking campaign, because we need to calibrate the detector with multiple energies in the X-ray tube lab with the gas mixture we are currently using.

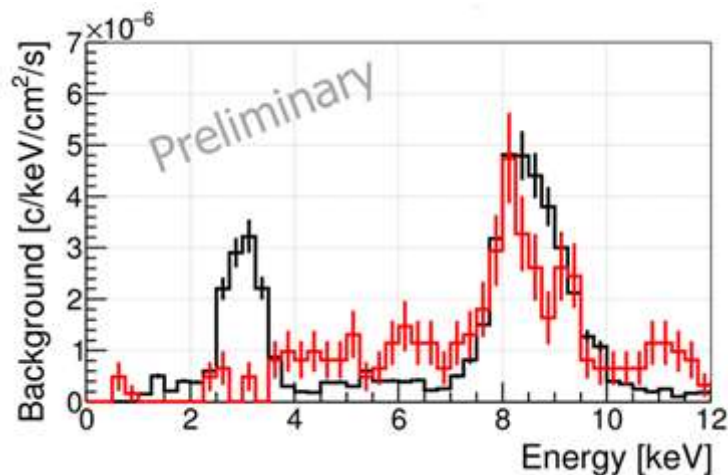


Figure 4.3: Background spectrum of the SRMM detector during 2015 (black) and 2020/2021 (red). The peak at  $\sim 3\text{keV}$  corresponds to Ar fluorescence and the  $\sim 8\text{keV}$  to Cu fluorescence. More than half of the background counts in the 2–7keV region are in the 3keV peak. Replacing Ar by Xe in the detector (red) makes this peak disappear and presumably further reduce background. In addition, the contribution from the  $\beta$ -decay of the naturally occurring  $^{39}\text{Ar}$  isotope, estimated to about  $10^{-7}$  counts/keV/s/cm<sup>2</sup>, would be avoided. The red curve shows the preliminary background spectrum for 1 track events in runs with xenon, where no peak is seen in the 3 keV range.

#### 4.7 Low gain runs

During the last days, about 60 hours of low gain background runs have been taken. The aim of these is to see high energy events such as alphas from Rn, and to quantify their effect especially in the low energy range of the spectrum. This study is in process and more statistics would be desirable.

## 5 InGrid/GridPix detector – Search for low energy solar ALPS

The CAST InGrid detector is a gaseous low-background X-ray detector based on a GridPix structure as gas-amplification device. A GridPix structure consists of a Micromegas-like aluminum grid mount 50  $\mu\text{m}$  above the surface of a charge-collecting pixel CMOS-ASIC, in this case the TimePix ASIC. A second generation CAST Ingrid detector has been taking solar tracking data in 2017/18 in the focal plane of the LLNL IAXO-pathfinder X-ray telescope. The detector consisted of seven GridPix structures. The central GridPix was positioned in the focal spot of the telescope and was surrounded by six GridPixes acting as veto and augmented with two scintillator based external veto detectors as well as an FADC readout of the signal induced of the grid. The detector was equipped with an ultra-thin 200nm X-ray entrance window significantly improving efficiency in the  $<1$  keV energy range. Thus the detector targets the search for X-rays from the conversion of low-energy solar axions or ALPS (e.g. Chameleons) in the CAST magnet. In the case of solar axions, such low energies are expected in the case of their production in the sun through the axion-electron coupling. Given the recent observation of an excess in low-energy electron recoils by the XENON1T experiment, the search for axion-electron-produced solar axions received refreshed interest.

The remaining activity of the group who developed, built and operated the CAST InGrid detector (U Bonn) is in the calibration and analysis of the solar tracking and background data taken in 2017 and 2018. Due to lack of funding, the analysis is carried out part-time by a single student which may explain the slow (but steady) progress. The goal is to improve the sensitivity to solar chameleon production (superseding the previous CAST limit achieved with the first-generation InGrid detector) and publish this result. In addition, if the sensitivity of the data can be further improved using refined software suppression of the background, there may be sensitivity to the axion-electron coupling beyond the current CAST limit. In that case, a second result is in the pipeline to be published.

Among the open items listed in the previous annual SPSC report (Sept. 2020) considerable progress has been made in the following areas.

### 5.1 Stability of energy calibration

The median energy of individual clusters in the background and calibration data, binned over time, is expected to be flat. It was observed that both in background and calibration runs, this quantity fluctuates significantly on the time scale of hours, as shown in Figure 5.1 (left) for the 2017 data taking period.

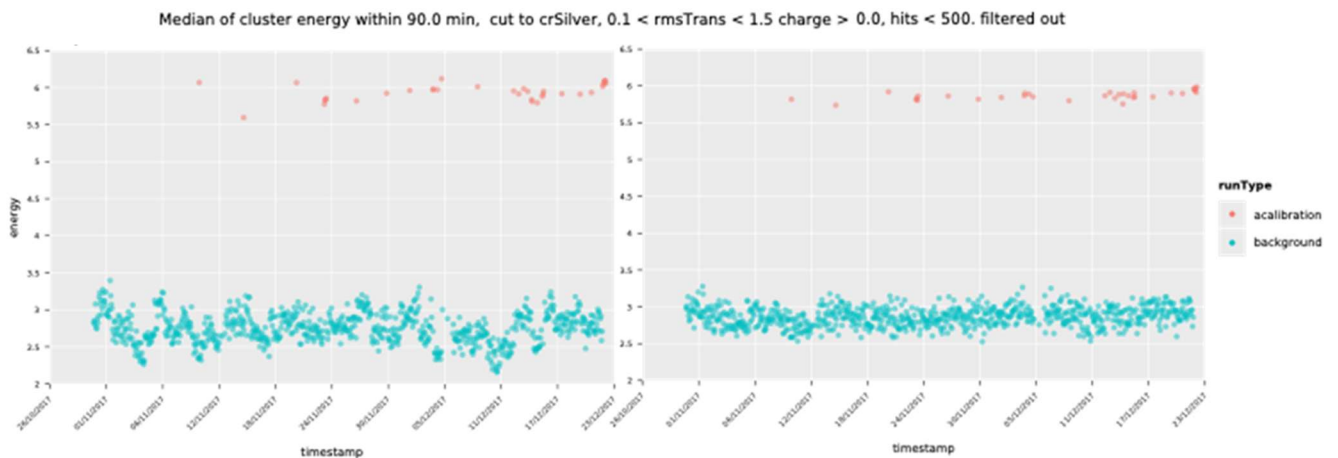


Figure 5.1: Median cluster energy vs. time (for 90 minute intervals per point). Only events with less than 500 active pixels are included to reduce bias from occasional highly ionizing particle events. Only clusters in the “silver” fiducial region with a weak cut on RMS transverse (“photon-like”) are included. Cyan dots are background runs, red dots are calibration runs. Left: original calibration procedure; Right: new calibration procedure which determines the actual gas gain more frequently (here: in 90-minute bins).

The suspected reason for the time-dependence is a time-dependence of the gas gain, e.g. due to temperature, pressure or other residual gas contamination.

The default energy calibration works as follows in a simplified form:

- (1) Compute the gas gain of each run for both background (typically 2-4 day long) and calibration (2h long).
- (2) Fit all  $^{55}\text{Fe}$  spectra of the calibration runs, including the escape peak. Photo and escape peaks are used for a linear energy calibration (i.e. charge-to-energy conversion factor).
- (3) From all linear fits of the calibration runs, perform a linear fit of all gas gains versus the calibration factors of each individual calibration. This yields a function which maps gas gain values to energy calibration factors.

Use the computed function of (3) to calculate the energy for each cluster in background and calibration runs, by using the gas gain value computed for each run as the input.

This calibration procedure ensures to be insensitive to gas gain variations from run to run. If the gas gain, however, changes within a run, the calibration becomes unreliable as can be seen in Fig. 1 left. To mitigate the effect, we now determine the gas gain at regular time intervals (here: every 90 min). This time is long enough to collect sufficient statistics in the “Polya” distribution, i.e. the charge per pixel distribution. On the other hand, the time is short enough compared to the typical time scale at which significant gas gain changes occur. The energy calibration then is modified to use the corresponding gas gain values for each cluster as an input to the fit function derived in point 3. As can be seen in Figure 5.1 (right), this new procedure results in a much flatter median cluster energy over time. The observed statistical fluctuation of the median cluster energy can be minimized by optimizing the time bin width where 90 min appear an optimal compromise. Longer time scales would introduce visible time variation. In the course of this study, it was also observed that the occasional occurrence of very highly ionizing tracks (e.g. from alpha particles) may lead to a bias in the “Polya” distribution towards large charge depositions. Single events led to outliers in the energy calibration. These events, which can be easily identified are now removed from the analysis, which also leads to a significantly more stable energy calibration run-by-run.

Based on this improved calibration procedures, the analysis will now be repeated step by step with possible fixes or improvements on the way.

## 5.2 Optimization of energy-dependent likelihood selection

It was observed since long, that for energies below  $\sim 1\text{keV}$  the observed background level (after full software rejection) is higher than above 1 keV. This can be understood since the number of electrons is proportional to the energy making it harder to distinguish a low-energy deposition from background. Previously, the likelihood cut to select candidate events was tuned such that for each energy bin the efficiency remained constant at 80%. We now studied more systematically if this tuning is optimal in terms of sensitivity. We varied the likelihood cut bin-by-bin and the expected limit on  $g_{ae}$  (for fixed  $g_{a\gamma}$ ) in each bin (for the current, preliminary overall settings of the analysis). For most high-energy bins, there was only a weak dependence on the precise choice of the likelihood cut. However, variations of the cut in the  $<1\text{ keV}$  bins show a significant dependence. Preliminarily, a reduction of the software efficiency from 80% to 60% (i.e. a stronger likelihood cut) yields a  $\sim 15\%$  stronger limit on  $g_{ae}$ . This observation led us to the conclusion that it is worth to invest more effort in the energy-dependent optimization of the likelihood selection, which is ongoing.

## 5.3 Advancement towards more modern statistical interpretation (profile likelihood)

So far, the statistical interpretation of the analysis is done with a simple frequentist  $CL_s$  interpretation (TLimit), which is not ideal, e.g. for the inclusion of systematic uncertainties. We are in the course of changing to RooStats/RooFit/HistFactory based profile likelihood fitting of the data to signal and

background taking advantage of the possibility to implement systematic uncertainties more rigorously via nuisance parameters. This approach makes it also more easy to make better use of the spatial distribution of the observed events. The background level increases considerably toward the corners of the chip. This is currently only reflected by considering a fixed fiducial region (“gold region”) in the center of the chip. However more position information can be exploited included the expected signal distribution from solar axions and/or solar chameleons.

#### **5.4 Further improvements**

Preliminary studies had shown that the impact of simple veto algorithms from the six surrounding chips, from the scintillators and from the FADC grid readout is only moderate. However, in particular for the six outer chips, not all information has been exploited so far. A new attempt will be made to optimally use this information.

In summary, the analysis of the CAST Ingrid data is progressing slowly but steadily. Surely one, ideally two more publications with physics results are planned. A technical publication on the second generation CAST Ingrid detector is also in preparation. Given the recent progress, the finalization of the analysis by the end of 2021 appears feasible.

## **6 KWISP – Chameleon Search with an opto-mechanical detector**

The KWISP opto-mechanical force sensor, in its latest 3.5 version, is now online at the CAST experiment at CERN after a long delay in activities caused by the persisting health emergency. During this suspension the efforts were directed to data analysis instead. At present the data taking has been restarted and we expect to collect about 10 hours of sun-tracking data.

### **6.1 Introduction**

Recall that the chameleon search at CAST uses the existing X-ray telescope to focus the hypothetical solar chameleon flux on the sensitive element of the KWISP opto-mechanical detector and does not require a magnetic field. Therefore it is operated in a parasitic fashion with respect to the ongoing axion searches.

We report here on the status and activities conducted in the last period. In particular the membrane longitudinal position control was put in place and a completely new chameleon chopper was designed, built and installed in the system. In parallel the data from the previous measurement campaigns were fully analyzed.

### **6.2 KWISP 3.5 set-up**

KWISP 3.5 is based on a high finesse Fabry-Perot (FP) resonant cavity with a thin membrane made of stoichiometric silicon nitride placed in the middle. This setup transduces sub-nm displacements of the membrane into a cavity detuning which is easily detected in the frequency locking feedback loop. Here the displacements might have been caused by the radiation pressure of particle beam and can be translated into a force by an equivalent spring constant of the membrane which is frequency dependent. This mechanical impedance was separately determined in a dedicated setup based on a Michelson interferometer [1]. A special feature of the KWISP 3.5 setup is a chameleon chopper placed in the chameleon beam before the detector. The chopper modulates the beam at a predetermined frequency thus allowing for easy identification of the interaction of the chameleon beam with the sensor in the detuning spectra of the FP cavity.

### 6.3 Recent upgrades

KWISP 3.5 is equipped with an auxiliary 532 nm laser beam used to obtain a direct force calibration of the sensor. The injection of the green laser through an optical fiber has been realized (see Figure 6.1) and tested at CAST. For this purpose a new green laser has been acquired and installed with the effect of enhancing the coupling efficiency into the transport fiber. This allows for an accurate online determination of the force acting on the membrane. The calibration is performed with a beam of particles, photons, of known intensity which is also modulated in time at a determined frequency. This can be seen as a peak at a known frequency in the detuning spectrum. The previous chopper, based on a digital micro-mirror device (DMD), has been substituted with a disk coated with a platinum pattern (see Figure 6.2) thus improving its efficiency since it has almost 10 times higher density than the DMD coating. Besides the density, also the geometrical efficiency is enhanced since it covers the entire projected membrane surface. Also the chopping frequency is increased thus allowing for using less rumorous parts of the detuning spectrum.

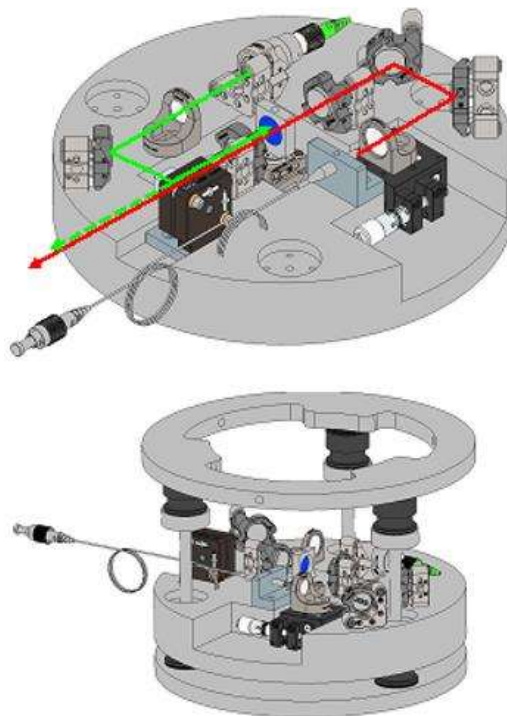


*Figure 6.1: KWISP 3.5 version with fiber launched calibration beam at 532 nm (green line). The optical path of the infrared sensing beam is shown in red.*

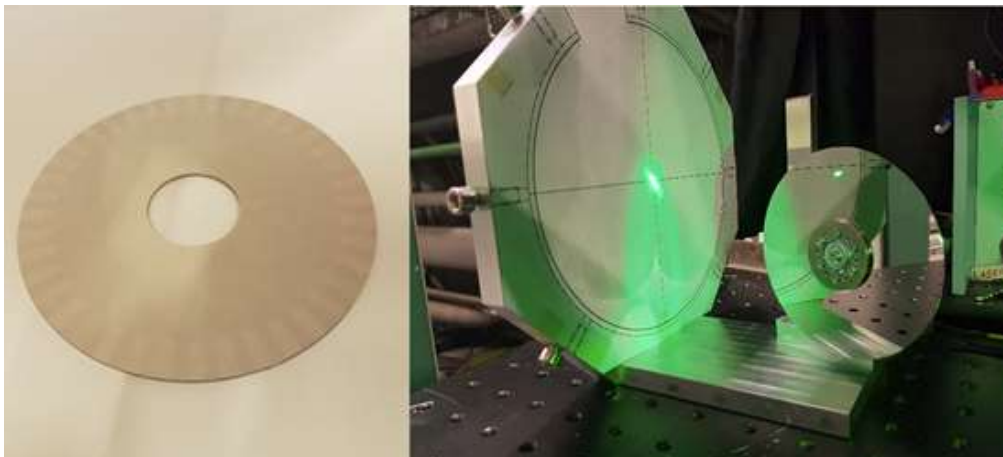


*Figure 6.2: New platinum pattern coated chameleon chopper disk (see text).*



## 6.4 Data taking

Two weeks of data taking, corresponding to up to 10 hours of usable sun-tracking data, have been carried out to the end of May 2021 with the upgraded setup. A higher sensitivity and results of improved accuracy are expected.

## 6.5 Results

The data analysis of the solar tracking campaign at CAST in 2020 with the KWISP detector (version 3.5) has been concluded. Utilizing a dedicated Python script in total about 10 hours of solar tracking data and 20 hours of background data were analyzed. The script calculates the FFT for a specified chunk of data and, in a small region around the known calibration and chopper frequency, checks for any signal above background. In case of a  $5\sigma$  excess the corresponding SNR is calculated. Taking into account the applied laser intensity the SNR acquired from the calibration data yields the sensitivity of the detector. In the absence of a signal at the chopper frequency the minimum detectable force is derived from the background noise level by considering the previously obtained sensitivity. Following this procedure, each set of data corresponding to a single solar tracking shift was analyzed. In a further step the data was combined and reevaluated again in the same manner. The results of the single day analysis showed that the detector sensitivity has not been constant over time. In fact, combining all data did not improve the result compared to the single data set of the 14th of August where the sensitivity has been the best. The comparison between the single day and full data set is illustrated in Figure 6.3. From the single day data set a force sensitivity of  $S = (50 \pm 20)$  pN/ $\sqrt{\text{Hz}}$  was determined. Due to the absence of a signal over background in the corresponding data at the measured chopper frequency  $f_{chop} = (4179.645 \pm 0.005)$  Hz, which was set independently, (see Figure 6.4) a minimum detectable force of  $F_{lim} = (2.0 \pm 0.8)$  pN could be deduced. A detailed study of the DMD chopper module used during the solar tracking campaign revealed a suboptimal efficiency, leading to a cut-off of the accessible chameleon spectrum at the upper and lower bounds of the chameleon matter coupling. Nonetheless, calculating the chameleon flux reaching the detector and taking the chopper efficiency into account as well as the derived force limit lets us place an exclusion limit in the beta-gamma-beta-matter parameter space. The resulting chameleon exclusion plot, with a comparison to the previously published result (blue) of KWISP [2] is shown in Figure 6.5. The projected exclusion for the data taking in 2021 utilizing an improved chopper is shown as well (red). A first glimpse at the 2021 data of a single solar tracking indicates a sensitivity of  $S = (27 \pm 2)$  pN/ $\sqrt{\text{Hz}}$  and a force limit of  $F_{lim} = (1.10 \pm 0.09)$  pN.



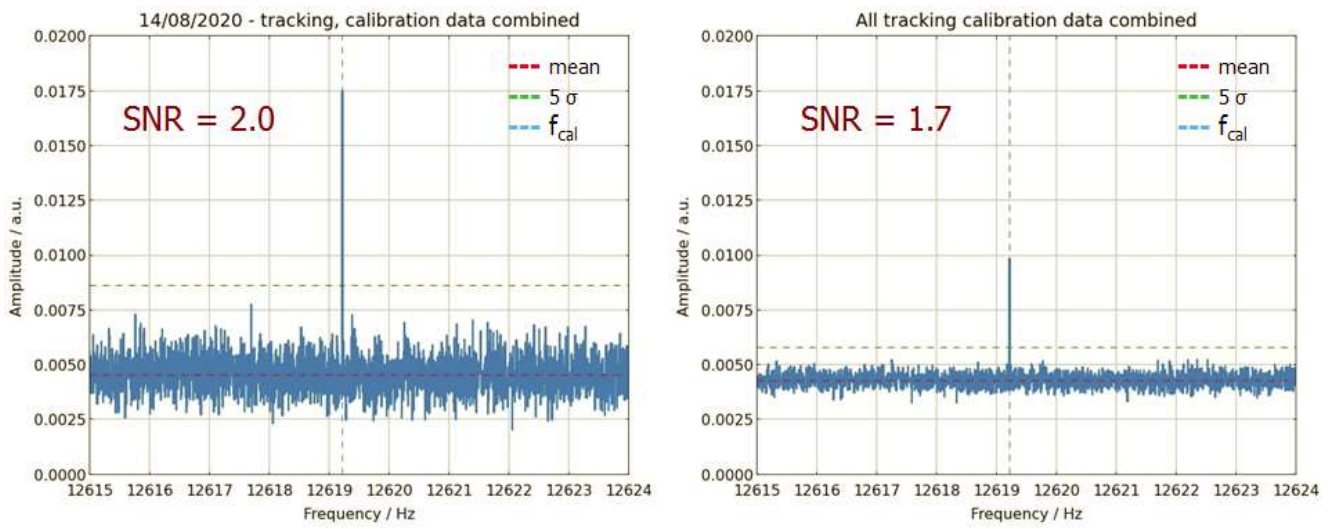


Figure 6.3: Comparison of calibration signal ( $f_{cal} = 12619.2$  Hz) for two different shifts.

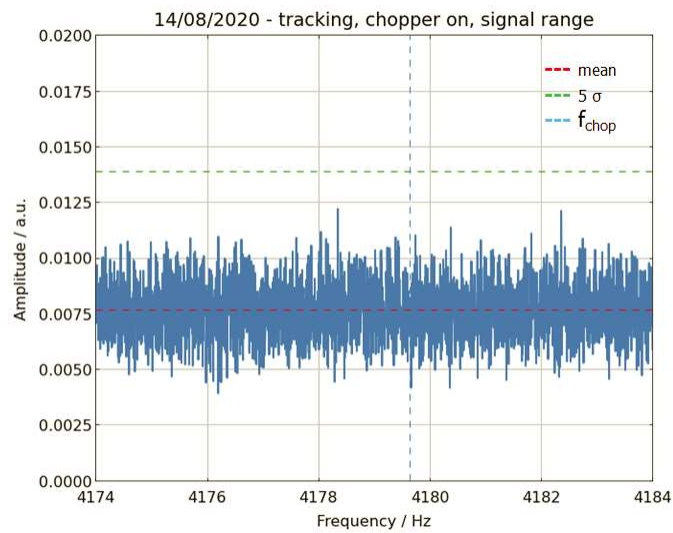


Figure 6.4: Signal range data used to derive the force limit. A chameleon signal should appear at the indicated chopper frequency of  $f_{chop} = 4179.645$  Hz.

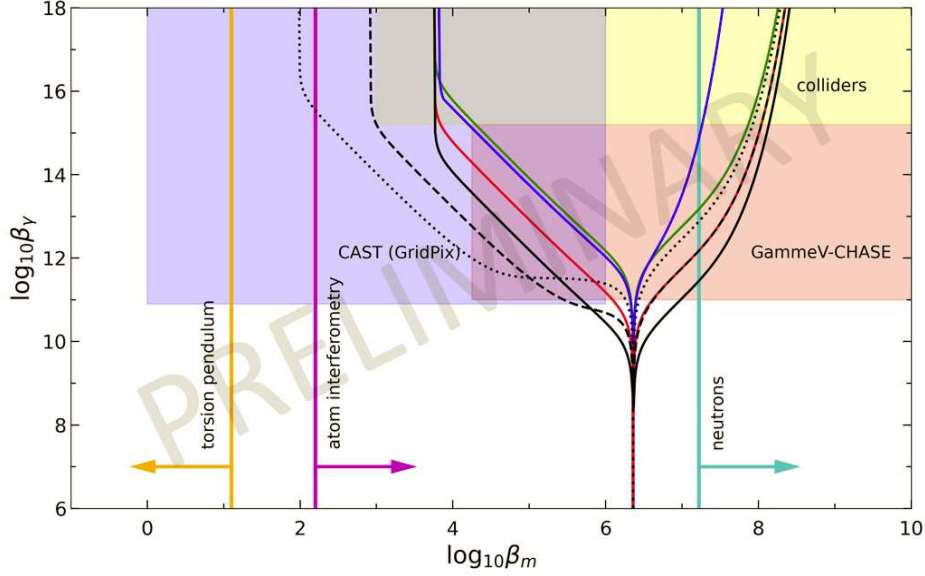


Figure 6.5: Preliminary chameleon exclusion plot. Published KWISP data [2] are plotted in green. The 2020 data are presented in blue color, while the red line shows the projection for the currently gathered 2021 data, assuming a sensitivity of  $S = (27 \pm 2) \text{ pN}/\sqrt{\text{Hz}}$ . The black line gives a projection for 12 months data taking (90 min/day) in the same conditions of 2021. Given only a single solar tracking but otherwise the same conditions the dashed and dotted black lines indicate the limits for the case of using a platinum coated sensing membrane at  $5^\circ$  and  $1^\circ$ , respectively. The other bounds, shown for comparison, are listed in Figure 12 of reference [2].

## 6.6 Conclusions

The upgraded KWISP 3.5 chameleon sensor is taking data at CAST parasitically with respect to the axion haloscopes. Analysis of the 2020 data evidenced no chameleon signal, however KWISP 3.5 set improved bounds in the chameleon parameter space. The current sensitivity of  $S = (27 \pm 2) \text{ pN}/\sqrt{\text{Hz}}$ , in case of continued data taking, will allow covering an unexplored region in the  $\beta_\gamma$ - $\beta_m$  space between  $5.7 < \log\beta_m < 7.0$  and  $11 > \log\beta_\gamma > 9$ , excluding resonances. Further planned upgrades include coating the sensing membrane with a platinum layer in order to increase its density, which will extend the sensitivity to smaller  $\beta_m$  values. Assuming the same conditions as for the current detector operation as well as a single solar tracking the projected exclusion limit is shown as dashed black line in Figure 6.5. Even smaller  $\beta_m$  values could be reached by placing the platinum coated membrane at a smaller angle with respect to the incident chameleon flux. For otherwise unchanged parameters, and considering the smaller effective area, this will be accompanied by a reduced sensitivity to values for  $\log\beta_m > 5$ , which is indicated as dotted black line in Figure 6.5.

## References

- [1] M. Karuza, D. Božičević, G. Cantatore and M. Vretenar, "Radiation Pressure Sensor," 2020 43rd International Convention on Information, Communication and Electronic Technology (MIPRO), 2020, pp. 1890-1893, doi: 10.23919/MIPRO48935.2020.9245357.
- [2] S. Arguedas Cuendis et al., "First results on the search for chameleons with the KWISP detector at CAST", Phys. Dark Univ., **26** (2019), 100367.